

Equilibrium evaporation coefficients quantified as transmission probabilities for monatomic fluids

Citation for published version (APA):

Wolf, M. C. W., Enright, R., Gaastra-Nedea, S. V., & Frijns, A. J. H. (2024). Equilibrium evaporation coefficients quantified as transmission probabilities for monatomic fluids. *Physics of Fluids*, 36(6), Article 062117. <https://doi.org/10.1063/5.0213744>

DOI:

[10.1063/5.0213744](https://doi.org/10.1063/5.0213744)

Document status and date:

Published: 01/06/2024

Document Version:

Accepted manuscript including changes made at the peer-review stage

Please check the document version of this publication:

- A submitted manuscript is the version of the article upon submission and before peer-review. There can be important differences between the submitted version and the official published version of record. People interested in the research are advised to contact the author for the final version of the publication, or visit the DOI to the publisher's website.
- The final author version and the galley proof are versions of the publication after peer review.
- The final published version features the final layout of the paper including the volume, issue and page numbers.

[Link to publication](#)

General rights

Copyright and moral rights for the publications made accessible in the public portal are retained by the authors and/or other copyright owners and it is a condition of accessing publications that users recognise and abide by the legal requirements associated with these rights.

- Users may download and print one copy of any publication from the public portal for the purpose of private study or research.
- You may not further distribute the material or use it for any profit-making activity or commercial gain
- You may freely distribute the URL identifying the publication in the public portal.

If the publication is distributed under the terms of Article 25fa of the Dutch Copyright Act, indicated by the "Taverne" license above, please follow below link for the End User Agreement:

www.tue.nl/taverne

Take down policy

If you believe that this document breaches copyright please contact us at:

openaccess@tue.nl

providing details and we will investigate your claim.

Equilibrium evaporation coefficients quantified as transmission probabilities for monatomic fluids

M.C.W. Wolf ^{1,*}, R. Enright ², S.V. Gaastra-Nedea ¹, A.J.H. Frijns ¹

¹Eindhoven University of Technology, PO Box 513, 5600MB Eindhoven, the Netherlands

²Seguente Inc., Melbourne, FL 32901 USA

Abstract

Equilibrium molecular dynamics (MD) simulations are used to investigate the liquid/vapor interface where particle exchange between the liquid and vapor phase is quantified in terms of the evaporation and condensation coefficient. The coefficients are extracted from MD simulations via a particle counting procedure. This requires defining a *vapor boundary position* for which we introduce an accurate and robust method and present a comparative study with existing methods from the literature. This novel method relies on the behavior of the flux coefficient within the interphase region by scanning the position of a particle sink boundary from the liquid towards the vapor phase. We find a distinct local maxima is attained on the vapor side of the interphase that is identified as the vapor boundary position based on an interpretation of transmission probability theory and the Kullback-Leibler divergence. The ratio of the evaporation flux to the outgoing flux at this location is defined as the evaporation coefficient. This method retains the simplicity of existing methods but eliminates several disadvantages. We apply this method to MD simulations of monatomic fluids neon, argon, krypton and xenon. We observe a correlation between the molecular transport parameter appearing in transmission probability theory and the characteristic interface fluctuation length scale from capillary wave theory. This gives an expression for the evaporation coefficient that agrees well with values extracted from MD using the particle counting procedure. Compared to existing methods, the evaporation/condensation coefficient is determined more accurately for temperatures between the triple and critical points.

1 Introduction

Phase change at the liquid/vapor interface, i.e., evaporation and condensation, is a ubiquitous process with many applications in different fields including biology, astronomy, physics, chemistry and engineering(1). Accurate models and boundary conditions to describe the transfer of mass and energy across the liquid/vapor interface have become increasingly important in recent years(2). Understanding the process of evaporation and condensation is challenging, but in principle molecular dynamics (MD) can describe this precisely. However, due to the large computational cost of MD, practical modeling typically consists of a multiscale approach in which continuum models, e.g. Navier-Stokes, and gas kinetics models(3), e.g. BGK scheme(4), S-model(5; 6) and DSMC(7; 8), are used to capture heat/mass transfer in the bulk. MD can be used to study the liquid/vapor interface on the molecular scale to obtain the parameters appearing in the kinetic boundary condition (KBC) for the vapor phase. In particular, accurate calculation of evaporation/condensation coefficients ($\alpha_{e/c}$) and liquid temperature (T_L) appearing in the KBC as a function of system operating conditions are of particular interest in order to refine predictive models. Different techniques have been demonstrated in the literature to calculate these coefficients and liquid temperatures (9; 10; 11).

However, the wide range of evaporation coefficients found in the literature (9; 12; 13; 14; 15) makes it difficult to define a unique coefficient for each operating condition. A typical model that shows sensitive agreement to MD depending on α_e , α_c and T_L is the S-model (16; 17). Discrepancies up to 10% in the energy flux were obtained corresponding to ± 0.1 variation in evaporation coefficient or $\pm 1K$ variation in liquid temperature. This was traced back to the

*Corresponding author
Email address: m.c.w.wolf@tue.nl

precise location of the so-called liquid and vapor boundaries which are used to extract the evaporation/condensation coefficients from the MD simulations.

1.1 Evaporation coefficient and existing methods

The evaporation coefficient α_e is defined as the fraction of evaporated particles to the total outgoing particles from the condensed phase(9). Similarly, the condensation coefficient α_c is the fraction of particles which condense to the total colliding particles on the condensed phase. For the case of zero net mass flux in the system, the evaporation and condensation coefficient are equal(11), i.e., $\alpha_e = \alpha_c$. The part $(1 - \alpha_c)$ or $(1 - \alpha_e)$ represents the fraction of particles which reflect back into the vapor or condensed phase, respectively. At the molecular level, these coefficients are defined as,

$$\alpha_e = \frac{\langle J_{evap} \rangle}{\langle J_{evap} \rangle + \langle J_{ref} \rangle} = \frac{\langle J_{evap} \rangle}{\langle J_{out} \rangle}, \quad \alpha_c = \frac{\langle J_{cond} \rangle}{\langle J_{cond} \rangle + \langle J_{ref} \rangle} = \frac{\langle J_{cond} \rangle}{\langle J_{coll} \rangle} \quad (1)$$

where $\langle J_{...} \rangle$ is the time-averaged mass fluxes of the evaporating, condensing, outgoing, colliding and reflecting particles (10). To properly account for these fluxes in MD simulations, it becomes necessary to define liquid and vapor boundaries in the interphase region (see Fig.1). Here, the liquid boundary is considered as the end of the liquid phase and the vapor boundary as the beginning of the vapor phase. Between these boundaries, in a region of rapidly varying mean density, the interphase is defined.

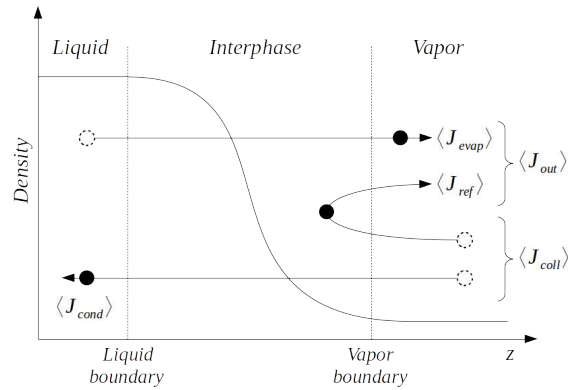


Figure 1: Schematic of the liquid/vapor interphase and corresponding mass fluxes adapted from Kobayashi(10). Reproduced with permission from Heat Mass Transfer 52, 1851 (2016). Copyright 2016 Springer.

While the definition of the evaporation coefficient is straightforward, the difficulty lies in precisely defining the end of the liquid phase and the beginning of the vapor phase. Below we summarize several methods found in the literature to determine the equilibrium evaporation coefficient that attempt to address this issue or avoid it entirely.

Meland(11) and co-workers used a geometrical definition to locate the liquid boundary. They defined the liquid boundary as the position where a tangent line at $(\rho_\infty + \rho_{liq}^{max})/2$ in the mean mass density profile intersects the line given by ρ_{liq}^{max} . Here, ρ_∞ is the equilibrium vapor density far from the interphase and ρ_{liq}^{max} is the maximum density attained in the liquid phase. To obtain the mass density profile in the liquid/vapor interphase region, a hyperbolic tangent function (18) was fitted,

$$\rho(z) = \frac{\rho_v + \rho_l}{2} + \frac{\rho_v - \rho_l}{2} \tanh \left[\frac{2(z - z_m)}{w_t} \right] \quad (2)$$

with $\rho_{l,v}$ the corresponding mass densities, z_m the equimolar dividing surface(18) and w_t is the characteristic length over which the density varies. The vapor boundary position was defined using the Soave-Redlich-Kwong (SRK)

equation of state(19),

$$P_{SRK} = \frac{RT}{v-b} - \frac{a}{v(v+b)} \quad (3)$$

where P is the absolute pressure, T the absolute temperature, v the molar volume, R the universal gas constant and a, b are two fluid dependent parameters. The location of the vapor boundary was defined as the position near the interphase where pressure difference $|P_{MD} - P_{SRK}|$ becomes greater than the largest pressure fluctuation in the vapor phase, i.e. $\max|P_{MD} - P_{SRK}|$. Here P_{MD} is the vapor pressure obtained from MD simulations.

The advantage of this method is the simplicity of the respective macroscopic definitions for which no additional MD simulations are required. Its disadvantage is the somewhat ad-hoc definition for the liquid boundary and lack of physical interpretation. Furthermore, at low reduced temperatures the statistical fluctuations of the vapor pressure increases which makes accurate determination of the vapor boundary difficult.

Gu(9) and co-workers focused on a new procedure to address the difficulty encountered in the method of Meland. The method uses a microscopic approach in which the location of the liquid and vapor boundary are based on the mean number of interaction partners $\overline{N}_k(t)$ per particle in a bin k . Two criteria values, C_v and C_l , are set as the limit on $\overline{N}_k(t)$ to consider the fluid to be in the vapor or liquid phase. The criteria values equal the mean number of interaction partners per particle $\overline{N}_k(t)$ in their respective phases and were obtained from separate MD simulations of pure liquid and pure vapor for which the density correspond to the saturated density at the temperature of interest. When moving from the liquid to the vapor phase, the first bin for which $\overline{N}_k(t) < C_l$ is recorded as the bin in which the liquid boundary is located. Similarly, the vapor boundary is located in the first bin for which $\overline{N}_k(t) > C_v$ when moving from the vapor to the liquid phase.

In contrast to the method of Meland, there exists a physical interpretation for the definitions of the liquid and vapor boundaries based on the molecular structure of the liquid and vapor phase. However, the drawback is that two additional MD simulations were required to obtain the criteria values C_l and C_v . Furthermore, no accuracy regarding the values of C_l and C_v were given for the values determined by Gu(9). We have observed that the assessment of C_v becomes increasingly uncertain at low reduced temperatures due to poor statistics, i.e., low vapor number density. As shown in appendix A, for low reduced temperatures, $T/T_C \lesssim 0.6$, the standard deviation is similar to the C_v value, making the accuracy of the identified vapor boundary location questionable.

In contrast to Meland and Gu, **Ishiyama(12)** implemented a method that avoids the definition of the liquid and vapor boundaries. In this case, the equilibrium evaporation coefficient was defined by introducing the concept of the spontaneously evaporating mass flux $\langle J_{evap}^{sp} \rangle$. Spontaneous evaporation is defined as the evaporation of particles that occurs independently of the incident vapor particles and its mass flux is obtained from MD simulations of evaporation into vacuum. Hence, the coefficient is defined as,

$$\alpha_e = \alpha_c = \frac{\langle J_{evap}^{sp} \rangle}{\langle J_{out} \rangle_e} \quad (4)$$

where $\langle J_{out} \rangle_e = \rho_v \sqrt{R_{sp} T_L / 2\pi}$ is the outgoing mass flux at equilibrium state with ρ_v the vapor density, T_L the liquid temperature and R_{sp} the specific gas constant.

The advantage is that both liquid and vapor boundary locations do not have to be defined. At low temperatures, the vapor behaves as an almost ideal gas due to the small potential energy compared to its kinetic energy. Thus, the assumption of evaporation taking place independently of the incident particles is a reasonably good approximation. However, at higher temperatures the contribution of the potential energy in the vapor phase increases making this simplification questionable. Spontaneously evaporating particles should exhibit more resistance because of their interaction with incident particles from the vapor phase. It is expected then that $\langle J_{evap}^{sp} \rangle$ will overestimate the evaporating mass flux from equilibrium MD simulations and will affect the accurate determination of the evaporation coefficient at higher temperatures.

Generally, uncertainties in the position of the phase boundaries affect the evaporation coefficient obtained. This can be especially pronounced at low temperatures where statistical fluctuations in the vapor can be significant such that the vapor boundary position can have a large standard deviation. The sensitivity of the coefficient on the defined boundary positions has not been explicitly discussed, as far as we know.

The goal of present paper is to introduce a revised definition of the *vapor boundary position* that addresses the aforementioned challenges. We present a comparative study of the behavior of the evaporation coefficient when using different monatomic fluids and liquid/vapor boundary positions including the existing methods of Meland and Gu.

Here, all MD simulations are performed under equilibrium conditions (i.e. zero net mass flux). Monatomic fluids, namely neon, argon, krypton and xenon modelled as a truncated shifted Lennard-Jones fluid are used to reduce the complexity of the system.

To avoid confusion, the ratio of the evaporating/condensation flux to the outgoing/colliding particle mass flux (Eq.(1)) is termed the *flux ratio* $\alpha = J_{(evap/cond)}/J_{(out/coll)}$. Once the liquid and vapor boundary are identified, the flux ratio is equated to the evaporation/condensation coefficient, i.e. $\alpha = \alpha_{e/c}$.

This paper is structured as follows. The properties of the equilibrium molecular dynamics simulations are given in section 2. Section 3 introduce the procedure of the alternative method after which results regarding the interphase thickness, the transmission probabilities, and evaporation/condensation coefficients are given. Finally, conclusions are provided in section 4.

2 Molecular Dynamics simulation details

As described above, for all methods molecular dynamics simulations are required to study the behaviour of the liquid/vapor interface properties such as density, pressure, temperature, mass and energy fluxes. Software package LAMMPS(20) is used to perform the MD simulations. A new LAMMPS function was written to calculate the mass fluxes appearing in Eq.(1). This function calculates the number of particles passing through the area $\Delta x \Delta y$, at position z , every N_τ time periods. For all fluids, the intermolecular forces between the particles are calculated using the truncated and shifted 12-6 Lennard-Jones potential,

$$U(r) = 4\epsilon \left[\left(\frac{\sigma}{r} \right)^{12} - \left(\frac{\sigma}{r} \right)^6 \right] - 4\epsilon \left[\left(\frac{\sigma}{r_{cut}} \right)^{12} - \left(\frac{\sigma}{r_{cut}} \right)^6 \right], \quad r < r_{cut}; \quad U(r) = 0 \text{ for } r \geq r_{cut} \quad (5)$$

where σ is the molecular diameter and ϵ the interaction energy. Its values for the monatomic fluids are given in table 1, the cutoff distance $r_{cut} = 2.5\sigma(21)$.

Table 1: Lennard-Jones parameters for MD simulations and liquid properties, κ_b is the Boltzmann constant, T_t the triple point temperature and T_C the critical temperature.

	σ [Å](21)	ϵ/κ_b [K](21)	Mass [g/mol](22)	T_t [K](22) from NIST	T_C [K](22) from NIST	T_C [K] from MD	T_C [K](23; 24) $T_C \kappa_b / \epsilon = 1.085$
Neon	2.8000	39.83	20.18	24.56	44.49	43.10	43.22
Argon	3.3916	137.90	39.95	83.81	150.70	150.10	149.62
Krypton	3.6233	191.52	83.80	115.78	209.48	209.08	207.80
Xenon	3.9450 ^a	265.78 ^a	131.29	161.41	289.73	289.41	288.37

^afor xenon, large deviations (> 10%) in macroscopic properties were observed compared to NIST-REFPROP(22) when using the values provided by ref.(21), therefore ref.(25) was used for σ and ϵ .

The equilibrium simulations consists of a vapor confined between its condensed phase as shown in Fig.2. The temperature is controlled using a Nosé-Hoover thermostat(26; 27) with a damping constant of $100fs$ applied to a narrow slab on both liquid regions. Periodic boundary conditions are imposed in all three directions. Newton's equation of motions are solved with a time step of $\Delta t = 4fs$ and the mass fluxes are calculated every $N_\tau = 100$ time periods.

Steady-state is obtained by shifting all particles along the z -coordinate such that there is an equal number of particles in both liquid slabs. Measuring the difference in particle number ΔN between the liquid slabs, the particles are shifted over a distance Δz determined by (11),

$$\frac{\Delta N}{2} = n_{liq} A \Delta z \quad (6)$$

with A the cross section parallel to the interface and n_{liq} the particle density in the liquid phase. At different time steps during the simulation, the density profile along the z -coordinate is determined. To verify steady-state, the z -position of the mean density, i.e. $(\rho_l + \rho_v)/2$, within both interphases should remain constant. This also ensures that averaging

over multiple time steps does not broaden the interphase width.

The dimension of the simulation domain $L_x \times L_y \times L_z$ is important to avoid system size effects. According to Sides et al.(28), $L_x > 12.8\sigma$ and Braga et al.(29) $L_x > 10\sigma$. Furthermore, Watanabe et al.(30) mentioned that size effects can be ignored if L_x is sufficiently larger than the interphase thickness. To fulfill these requirements, the dimensions parallel to the interface are $L_x = L_y = 200\text{\AA}$ ($50.7\sigma - 71.4\sigma$, depending on the fluid) and orthogonal to the interface is $L_z = 440\text{\AA}$ ($111.5\sigma - 157.1\sigma$) for all temperatures and fluids. This also ensures that there is no unphysical interaction between the interfaces. The size of the thermostat regions is 20\AA ($5.07\sigma - 7.13\sigma$) and the distance between the thermostat and the interfaces is larger than 5σ to avoid any direct influence.

Initially, the liquid particles are randomly distributed in regions of size $\Delta z = 70\text{\AA}$ ($17.7\sigma - 25\sigma$) at the left and right side of the domain and the vapor particles in between with a density similar to the saturated liquid and vapor density at liquid temperature T_L . The number of particles varies between $N = 100,000 - 200,000$ which is larger than the minimum value of $N = 1000$ recommended by Trokhymchuk et al.(31). The liquid temperature range for all fluids varies between its triple temperature T_t and critical temperature T_C , except for argon, where three liquid temperatures below its triple point, $70K$, $75K$ and $80K$, are added.

To obtain equilibrium, the simulations are performed using three runs. The first run consists of thermalization using 10^6 steps. A Berendsen thermostat(32) with a small damping constant is applied to the liquid and vapor regions to allow the system to quickly reach the desired temperature. In the second run, the Nosé-Hoover thermostat is applied to the liquid regions shown in Fig.2. This ensures the correct simulation of a canonical ensemble (NVT), i.e. fixed number of particles, volume and temperature. In this run, another 10^6 steps are performed to ensure that the system has reached an equilibrium state. Equilibrium is verified by observing a constant potential energy as its relaxation time is slower than that of the system temperature (30). The third run of 5×10^6 steps calculates the mass fluxes of Eq.(1). In this run, particle information is stored every 200 steps. To calculate macroscopic properties, the domain is divided into bins of size 0.5σ (i.e. between 224 – 315 bins) along the z -coordinate and time-averaging over the output data.

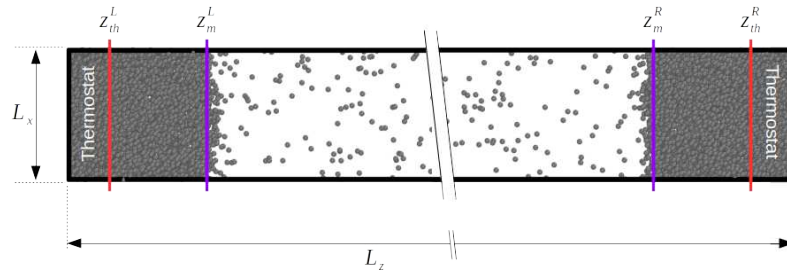


Figure 2: Schematic of the MD simulation domain. Here, $z_m^{L/R}$ is the equimolar dividing surface at the left and right interphase, $z_{th}^{L/R}$ defines the position where the thermostat ends in the liquid phase.

The liquid/vapor equilibrium MD simulations for neon, argon, krypton and xenon, are performed at different temperatures with its macroscopic properties such as liquid and vapor density, temperature, pressure and enthalpy change reported in appendix A. The critical temperature T_C for each fluid is obtained by a using the scaling law(18; 9),

$$\rho_l - \rho_v = \rho_0 \left(\frac{T_C - T}{T_C} \right)^\beta \quad (7)$$

where $\beta = 0.325$ is the universal critical exponent characterizing the density variation at the critical point. The unknown parameters ρ_0 and T_C were found by fitting the above equation to the density ρ and temperature T results of the equilibrium MD simulations. The critical temperatures are reported in the 7th column of Table 1. Its dimensionless critical temperature $T_C k_b / \epsilon$ for neon, argon, krypton and xenon are 1.0821, 1.0885, 1.0917 and 1.0889, respectively. This is in close agreement with previous work(23; 24) which reported a critical temperature of $T_C k_b / \epsilon = 1.085$ using a truncated and shifted LJ potential with cut-off distance $r_c = 2.5\sigma$. It is important to scale the temperature by its correct critical temperature, i.e. obtained from MD simulations, in order to make reliable comparison between results.

3 Results

3.1 Vapor phase

The vapor boundary identifies the separation between the interphase region and vapor region. A large mass density change and capillary waves(33; 34; 35; 36) are features of the interphase region whereas the behavior of the vapor region is isotropic at equilibrium. First, the transport behavior of argon vapor is discussed to support and complement our method to identify the vapor boundary introduced in the next section. Similar results are obtained for other monatomic fluids, i.e. neon, krypton and xenon.

Particle diffusion arising from particle random walk behavior (37) has been investigated for pure vapor using equilibrium and steady-state MD simulations. Two boundaries are used to distinguish between the "source" region defined before the first boundary and "sink" region after the second boundary. Diffusion particle density ρ_D and outgoing velocities U_D are calculated at the second boundary for different distances δ between the boundaries. The diffusion flux is defined as $J_D = \rho_D U_D$. Similarly, the outgoing mass flux for all vapor particles is defined as $J_{out} = \rho_v U_v$ with $U_v = \int_0^\infty v_z f_M(v) dv = \sqrt{RT/(2\pi)}$ where f_M is the Maxwellian velocity distribution. The ratios of the density ρ_D/ρ_v and velocity U_D/U_v are shown as a function of dimensionless distance δ/λ in Fig.3. Here, the mean free path is defined as $\lambda = \mu/\rho_v \sqrt{(\pi/(2RT))}$ with μ the vapor viscosity calculated using the expression given by Galliero et al.(38). Data points are obtained using different distances δ and argon vapor temperatures: $T_v = 70, 90, 110, 130K$ (thereby changing λ). When the distance between the boundaries is small, almost all of the particles leaving the first boundary diffuse to the second boundary. Hence, the density ratio is 0.5 and the outgoing velocity of diffusion particles is twice U_v . For increasing distance δ , the probability for particles to diffuse between the boundaries decreases. As a consequence, the density ratio converges to zero and the velocity ratio converges to a value of approximately 2.55. Furthermore, for $\delta/\lambda = 1$ the density ratio equals 0.25 whereas the velocity ratio is approximately 2.47 which is close to its final value ($100 \times 0.47/0.55 \approx 85\%$). When $\delta/\lambda > 1$, particles will have at least one collision on average which has negligible effect on the diffusion velocity U_D . The behavior of the density ratio ρ_D/ρ_v and velocity ratio U_D/U_v are both well fit by a logistic curve.

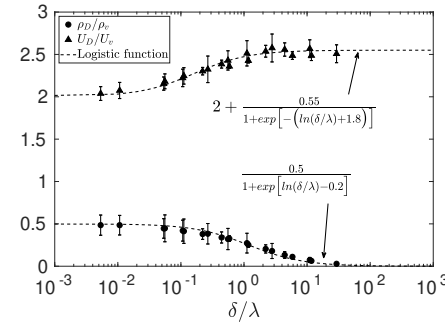


Figure 3: Argon density ratio ρ_D/ρ_v and velocity ratio U_D/U_v as function of δ/λ . Dashed lines corresponds to the fitted logistic functions.

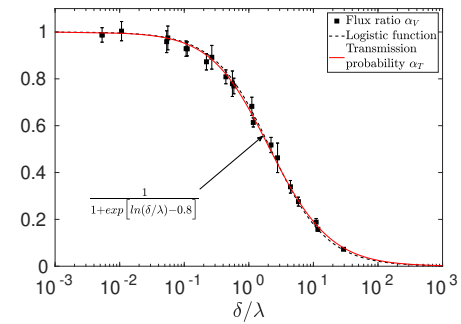


Figure 4: Argon flux ratio $\alpha_V = (\rho_D U_D)/(\rho_v U_v)$ as function of δ/λ . Dashed line corresponds to the fitted logistic function. Transmission probability α_T of Eq.(8) is shown as red solid line.

Essentially, the flux ratio $\alpha_V = J_D/J_{out}$ for the pure vapor phase defines the probability particles will diffuse over a distance δ , i.e. transmission probability. As shown in Fig.4, its behavior is also well described by a logistic curve. In the past, theories for the molecular flow transmission probability through circular cylindrical tubes have been developed by several investigators (39; 40; 41; 42; 43). These theories were developed for steady-state molecular flow for which the mean free path of the vapor is larger than the dimensions of the tube. This is generally the case for highly rarefied gases and evaporation at low pressures. Although the present MD simulations of pure vapor do not immediately appear to satisfy molecular flow conditions, the transmission probability theory is capable of describing the flux ratio α_V very well as observed in Fig.4. Here, the expression of Berman(44; 41) is used for the transmission

probability,

$$\alpha_T = \left[1 + \frac{F^2}{4} - \frac{F(F^2 + 4)^{1/2}}{4} \right] - \frac{[(8 - F^2)(F^2 + 4)^{1/2} + F^3 - 16]^2}{72F(F^2 + 4)^{1/2} - 288 \ln[F + (F^2 + 4)^{1/2}] + 288 \ln(2)} \quad (8)$$

where $F = L/R$ with L and R the length and radius of the concerned tube. By considering a particle with an average distance proportional to λ from the remaining vapor particles and travelling a distance δ , it will mimic molecular flow conditions through a circular cylindrical tube of radius R and length L . For the transmission probability theory the walls of the tube are considered to be solid implying their particles are at rest with respect to the laboratory reference frame. The average distance λ_{rest} a particle travels before colliding with the solid wall is proportional to the inverse of the average number density and scattering cross sectional area (45). In our case, the particles of the wall consists of the remaining vapor particles having an average velocity equal to the thermal velocity. Taking into account the relative velocity between the "wall" and vapor particles the average distance before colliding with wall is equal to the mean free path $\lambda = \lambda_{rest}/\sqrt{2}$ (46). Hence, to describe the flux ratio α_V using the Berman expression Eq.(8) the tube radius $R = \sqrt{2}\lambda$. The length of the tube is defined as the distance between the boundaries $L = \delta$.

3.2 Alternative method for determining the vapor boundary location

To accurately determine the vapor boundary position, we introduce an *alternative method (Wolf)* which relies on scanning the position of the particle sink boundary from the liquid boundary (particle source) towards the vapor phase in the direction perpendicular to the liquid/vapor interface. The liquid boundary position is determined using the method of either Meland or Gu. At each position of the particle sink boundary, the flux ratio α_{LV} is calculated as shown in Fig.5. When the position of the liquid z_{L_b} and particle sink boundary z_{V_b} overlap, i.e. $z_{L_b} = z_{V_b}$ the flux ratio equals unity. The flux ratio, α_{LV} , attains a minimum approximately halfway through the mean density profile and increases until the end of the interphase region where a *local maximum* in the vapor phase is consistently obtained.

Scanning the position of the particle sink from the liquid boundary towards the vapor phase, the mass flux components are obtained as shown in Fig.6. The outgoing mass flux shows similar behaviour as the mean density profile and remain constant in the liquid and vapor phase as expected. For the evaporating mass flux, a rapid decrease is seen after which a slow decrease follows. On the contrary, the reflecting mass flux has a rapid increase until the liquid density starts to decrease. It then reaches a minimum at the same location as the local maximum of α_{LV} before slowly increasing as the particle sink location moves further into the vapor phase.

We propose here that the **local maximum** in α_{LV} represents the actual location of the **vapor boundary**. We observe that its position is in very close agreement with the location at which the outgoing mass flux (J_{out}) becomes constant (see Fig.6), which is indicative of transport in a homogenous phase at equilibrium.

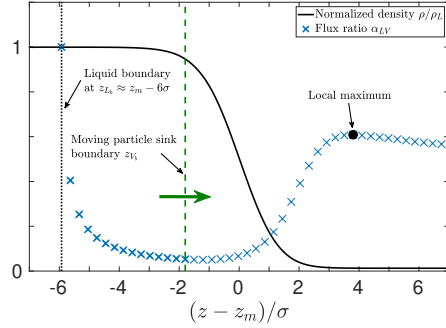


Figure 5: Profile of flux ratio α_{LV} by scanning the position of the particle sink boundary in z -direction z_{V_s} from an arbitrarily chosen liquid boundary (at a fixed position z_{L_b}) towards the vapor phase. Results correspond to argon at $T/T_C = 0.67$.

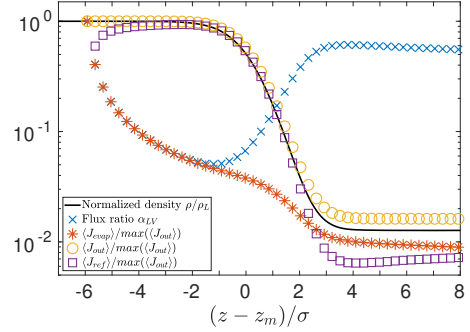


Figure 6: The evaporating, outgoing, reflecting mass fluxes J and flux ratio α_{LV} as function of position for an arbitrarily chosen liquid boundary position $z_{L_b} \approx z_m - 6\sigma$. Results correspond to argon at $T/T_C = 0.67$.

In Fig.7, the normalized evaporating particle density (ρ_{evap}/ρ) is plotted through the liquid/vapor interphase for different particle sink positions z_{V_s} . Here, the evaporating particles are the ones that are initially located before the liquid boundary z_{L_b} and diffuse over time towards the vapor region. For a constant mass density ρ the evaporating particle density is observed to decrease in an approximately linear fashion $[-9 < (z - z_m)/\sigma < -2]$. A slight change in slope is observed when moving through the rapid decaying mass density profile $[-2 < (z - z_m)/\sigma < 1.5]$. After which a strong attenuation of the density of evaporating particles is observed near the end of the interphase region $[1.5 < (z - z_m)/\sigma < 4]$. Finally, a linear decay is again observed when entering the vapor region $[4 < (z - z_m)/\sigma]$. Once an evaporating particle enters the vapor region, its behavior should be independent of its position within the vapor phase. The average density of the evaporating particles in the vapor region depends on the random walk (47) behavior of the particles and is described by the diffusion equation. Its steady-state solution is a linear function of position. Because the results are time independent, the linear decay of the evaporating particle density in both the homogenous liquid and vapor phases coincide with the behavior of the steady-state diffusion equation solution. The beginning of this linear decay of evaporating particle densities are within close proximity of the local maximum of α_{LV} .

When evaporating particles diffuse further into the vapor phase, their velocity distribution changes. Its mean velocity U_{evap} will increase since only the more energetic particles will have a higher probability to travel further into the vapor. This was also observed for the particle diffusion velocity U_D in pure vapor as shown in Fig.3. The average velocity distribution of all particle remains a Maxwellian distribution(49; 50). How the velocity distribution of evaporating particles differs from the Maxwellian through the interphase and vapor phase which can be quantified using the Kullback-Leibler divergence (48). For discrete probability distributions P and Q it is defined as

$$D_{KL}(P||Q) = \sum_{v \in \mathcal{V}} P(v) \log \left(\frac{P(v)}{Q(v)} \right) \quad (9)$$

Here, \mathcal{V} is the velocity space, P equals the Maxwellian distribution and act as a reference whereas Q is the velocity distribution of evaporating particles. Fig.8 depicts the Kullback-Leibler divergence as function of distance as well as the evaporating velocity U_{evap} scaled by the outgoing velocity U_v . In the liquid phase, D_{KL} is relative small implying both distributions P and Q are similar. Within the interphase region, D_{KL} changes more than 3 orders of magnitude after which a slower increase follows. A similar behavior is observed for the velocity ratio U_{evap}/U_v . Particles leaving the potential well of the liquid phase are very likely to increase the mean velocity of the evaporating particles very rapidly. As a consequence, U_{evap} primarily dictates the behavior of D_{KL} since U_v is constant. Again, the position at which the rapid increase of D_{KL} and velocity ratio U_{evap}/U_v changes to a slower increase is in close agreement with the position of the local maximum of α_{LV} . It marks the beginning of a different region, hence the start of the vapor phase.

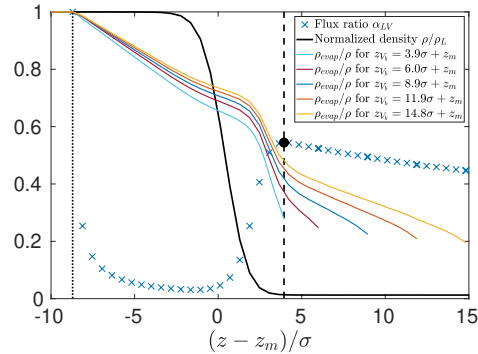


Figure 7: Normalized evaporating particle density profile (ρ_{evap}/ρ) and flux ratio α_{LV} for an arbitrarily chosen liquid boundary position at $z_{Lb} \approx z_m - 9\sigma$ and multiple particle sink positions z_{vb} for argon at $T/T_C = 0.67$.

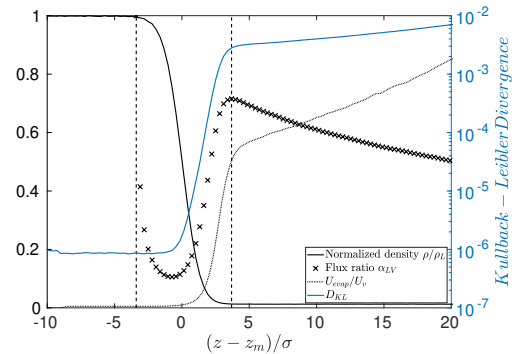


Figure 8: Argon at $T/T_C = 0.67$, Kullback-Leibler divergence D_{KL} (48) calculated using the Maxwellian velocity distribution and evaporating velocity distribution. Dashed vertical lines indicate the liquid boundary of Gu at $z_{Lb} = z_m - 3.4\sigma$ and local maximum at $z_{max} = z_m + 3.7\sigma$.

3.3 Interphase thickness

Before we investigate the interphase in terms of transmission probability theory, we must first define the interphase thickness. Figure 9 depicts the positions of the liquid boundary for the methods of Meland and Gu and the vapor boundary for Meland, Gu and the alternative method (Wolf). Positions of the liquid and vapor boundaries are similar for all fluids. The liquid boundary determined by the method of Meland is located closer to the interphase than Gu for all temperatures. For the vapor boundary, the results of the alternative method (Wolf) are similar to Gu, but differ substantially from Meland especially at high reduced temperatures. Thermal fluctuations broaden the interphase at higher reduced temperatures and therefore increase the distance of the liquid and vapor boundary position from the equimolar dividing surface z_m (51). Furthermore, the vapor boundary of Gu and Wolf are located at a similar distance from z_m as the liquid boundary of Gu.

In the mean-field theory, the density profile along the liquid/vapor interface is described by the tangent hyperbolic function of Eq.(2). Using capillary wave theory, the density profile is described using an error function in which the term $\tanh[2(z - z_m)/w_t]$ in eq.(2) is replaced by $\text{erf}[\sqrt{2}(z - z_m)/w_e]$ (28; 52). The error function predicts an interphase width $w_e \sim 6.5\%$ larger than w_t for temperatures between the triple and critical point consistently. In Fig.10, the interphase thickness ($z_{vb} - z_{Lb}$) is plotted as function of w_t . The symbols represent the MD results and the dashed lines a linear fit. It is observed that for each combination, the interphase thickness versus w_t is similar for all fluids. The thickness using Gu for the liquid boundary are generally larger than the method of Meland which is expected from Fig.9. Also, all four results of the thickness can be fitted very well by a linear relationship. The highest R-squared value is obtained using the method of Wolf for the vapor boundary position and the lowest when using the method of Meland. As discussed by Weeks(53), the interface thickness is linearly related to w_t with a constant depending on only the dimensions parallel to the interface. When the constant is unity, the interface thickness equals w_t . Because the dimensions parallel to the interface are equal for all temperatures and fluids, the method of Wolf ($V_b : Wolf$) will provide the most accurate definition of the interphase thickness according to Weeks(53). However, an almost equal accuracy is obtained for $L_b : Gu - V_b : Gu$ and a little less for the method of Meland ($L_b : Meland - V_b : Meland$). The inset in Fig.10 depict the thickness w_t as function of reduced temperature which is fitted by the scaling law(9),

$$d = d_0 \left(\frac{T_C - T}{T_C} \right)^{-\eta} \quad (10)$$

with parameters $d_0 = 1.29\sigma$ and $\eta = 0.65$. The scaling law describe the behavior near critical temperature and is therefore fitted to thickness corresponding to $T/T_C > 0.8$. Values of $\eta = 0.63 - 0.65$ are reported in literature (30; 23).

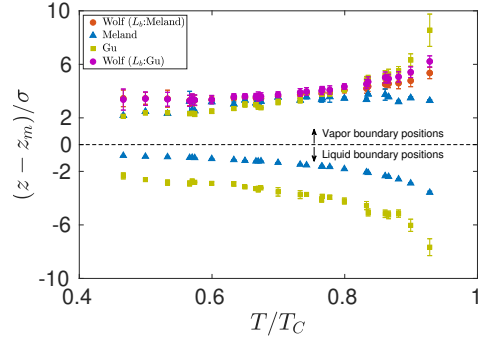


Figure 9: Liquid and vapor boundary positions as function of reduced temperature for all fluids. z_m is the equimolar dividing surface.

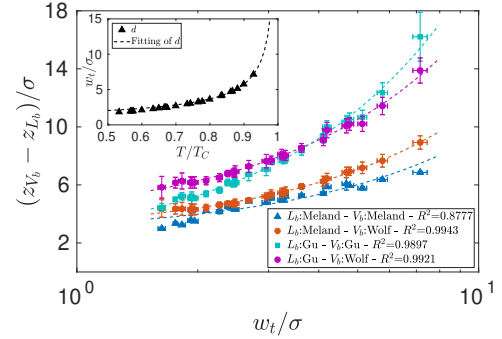


Figure 10: Interface thickness $(z_{V_b} - z_{L_b})$ as function of w_t from Eq.(2) for all fluids. For clarity we have plotted the data using a semi-log scale. Lines represent a linear fit with its R^2 value included in the legend. Inset: w_t as function of reduced temperature fitted by Eq.(10).

3.4 Transmission probabilities and the interphase

In the previous section 3.1, the behavior of the vapor phase was investigated by looking at the particle diffusion behavior. Quantified by the flux ratio α_V , good agreement with the transmission probability expression of Berman(44) Eq.(8) was shown in Fig.4 for all vapor temperatures and distances δ . In this context, if the local maximum in the flux ratio α_{LV} (see Fig.5) corresponds to the vapor boundary, we expect Eq.(8) to well fit the behaviour of α_{LV} from its local maximum into the vapor phase. This is confirmed in Fig.11, where we show the fit for different argon liquid temperatures $T_L = 70 - 130K$. It is observed that α_{LV} and Eq.(8) fit every well over the entire vapor region but start to deviate rapidly when crossing the local maximum (black dot). The starting location of the fitted Eq.(8) (i.e. when $\alpha = 1$) is labelled as the z_0 position. Hence, an excess length is defined $\delta_0 = z_{loc.max.} - z_0$ which represents the tube length L used in Eq.(8) to approximate the flux ratio at the local maximum. It accounts for a changing particle scattering behavior through the liquid/vapor interphase subjected to a rapid change in mean free path proportional to the inverse of the mass density. By shifting and scaling each flux ratio α_{LV} by its z_0 and λ , the behavior after the local maximum should collapse for all temperatures. This is shown in Fig.12 and demonstrates good agreement with Eq.(8), coinciding with the results of pure vapor shown in Fig.4.

Due to the excess length $\delta_0 > \delta$ a slight deviation between the evaporation coefficient and flux ratio in pure vapor is shown in Fig.13. Here, δ represents the interphase thickness for the liquid/vapor simulations (i.e. $\delta = z_{V_b} - z_{L_b}$) and the diffusion length for the case of pure vapor simulations (sec. 3.1). At low reduced temperatures, the interphase thickness δ is small and the mean free path λ large i.e. $\delta/\lambda \ll 1$. A ballistic transport of particles is obtained between the liquid and vapor boundary with an evaporation coefficient close to unity. When $\delta/\lambda \gg 1$, particles are subjected to an increasing number of collisions within the interphase. The probability of a particle crossing the liquid and vapor boundary decreases, resulting in a decreasing evaporation/condensation coefficient. In Fig.14, the density ratio ρ_D/ρ_v and velocity ratio U_D/U_v are depicted. Both density ratios ρ_D/ρ_v are very similar but the velocity ratio U_D/U_v results for the liquid/vapor simulations are shifted one order of magnitude to the right relative to the results of pure vapor.

This is the author's peer reviewed, accepted manuscript. However, the online version of record will be different from this version once it has been copyedited and typeset.

PLEASE CITE THIS ARTICLE AS DOI: 10.1063/1.50213744

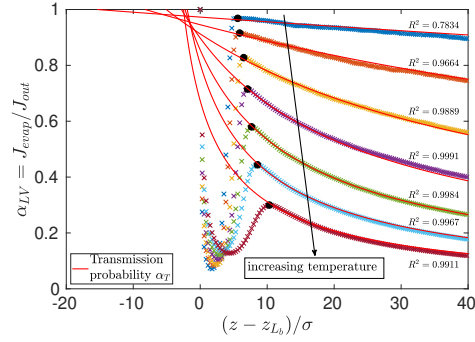


Figure 11: Argon flux ratio α_{LV} for different temperatures (70–130K, with increments of 10K). Transmission probability α_T of Eq.(8) (solid red lines) fitted to flux ratio in vapor region. Local maxima of flux ratios indicated by black dots.

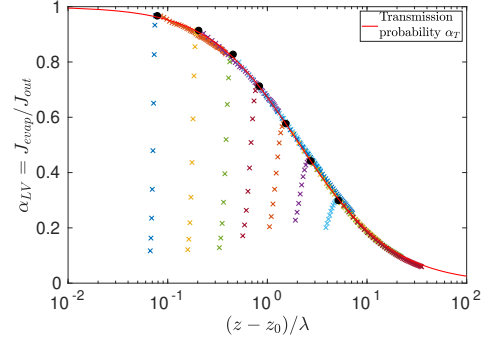


Figure 12: Argon flux ratio α_{LV} for different temperatures (70–130K, with increments of 10K) shifted by z_0 . Transmission probability α_T of Eq.(8) shown as solid red line. Local maxima of flux ratios indicated by black dots.

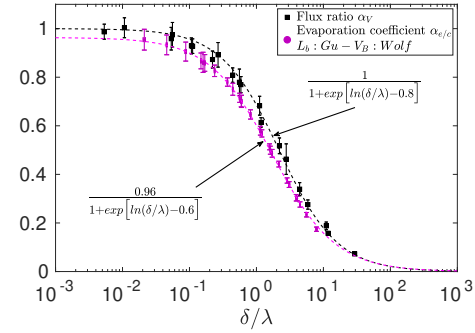


Figure 13: Evaporation/condensation coefficient $\alpha_{e/c}$ (for Ne,Ar,Kr,Xe) and flux ratio α_V (only argon) as function of reduced interphase thickness. Dashed lines corresponds to logistic functions.

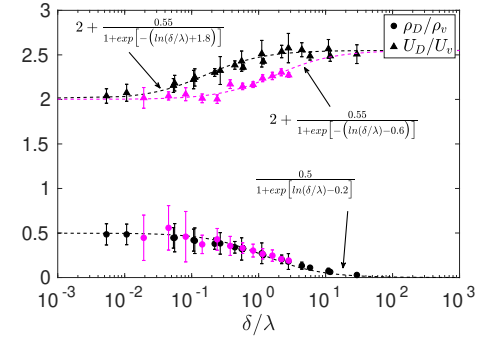


Figure 14: Argon density ratio ρ_D/ρ_v and velocity ratio U_D/U_v as function of δ/λ . Dashed lines corresponds to the fitted logistic functions. Black color: results pure vapor simulations (sec.3.1). Magenta color: results of liquid/vapor simulation with $L_b : Gu - V_b : Wolf$.

Finally, the position of the vapor boundary should be independent of the choice of the position of the liquid boundary. Moving the liquid boundary closer to the interphase region, i.e. $z_{Lb} \approx z_m - 6\sigma$ to $z_{Lb} \approx z_m - 3\sigma$ as shown in Fig.15, increases the value of the local maximum, which can be explained by the fact that when the liquid boundary z_{Lb} moves towards the vapor phase, more particles are considered to be in the liquid phase, i.e. particles for which $z \leq z_{Lb}$. Since the liquid particles are closer to the sink boundary, a particle has a higher probability to travel from the liquid to the sink boundary and vice versa (see Fig.1). Hence, this increases the mass flux of evaporating particles and reflects back into an increase of the flux ratio. The position of the local maximum remains similar, moving the liquid boundary over a distance of 6σ changes the location of the local maximum less than 0.5σ . Also this shows the strengths of our approach to define the vapor boundary position by looking at the position of the local maximum of α_{LV} .

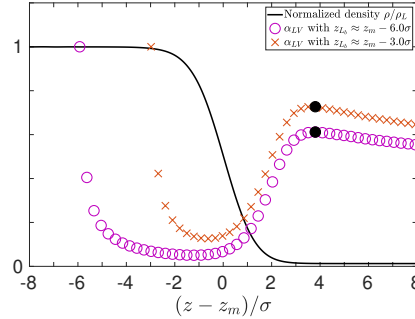


Figure 15: Influence of arbitrarily chosen liquid boundary positions $z_{L_b} \approx z_m - 6\sigma$ and $z_{L_b} \approx z_m - 3\sigma$ on the behaviour of the flux ratio α_{LV} for argon at $T/T_C = 0.67$. Black dots indicate the maximum value attained in the vapor phase.

3.5 Evaporation & Condensation coefficients

The evaporation/condensation coefficient describes the probability of a particle to travel from the liquid phase to the vapor phase (and vice versa) across the interphase region. As the temperature increases, the interphase thickness increases as shown in Fig.9, and the vapor mean free path decreases. Therefore, the probability of a particle to travel across the interphase region decreases when approaching the critical temperature. Hence, the evaporation coefficient approaches zero when the interphase thickness diverges (i.e. $T/T_C \rightarrow 1$).

Figure 16 depicts the evaporation coefficient as function of reduced temperature. A clear distinction is observed when using the vapor boundary of Wolf instead of Meland or Gu. The former provide a monotonic decay of the coefficients over the entire temperature range whereas the latter only after $T/T_C > 0.6$. Liquid and vapor boundary positions of Meland are located closer to the interphase, particles have a higher probability to travel across the interphase and thus provide a higher coefficient for most temperatures. The results of Meland are similar to Gu ($L_b : Gu - V_b : Gu$) but shifted approximately 0.1 upwards.

At lower reduced temperatures the results of $V_b : Gu$ start to deviate significantly from $V_b : Wolf$. This can be related to the low accuracy of the criterium value C_v as shown in the tables of appendix A and thus a less accurate position of the vapor boundary. Furthermore, the coefficient increases more rapidly between its minimum at $(z - z_m)/\sigma \approx 0$ and maximum at $(z - z_m)/\sigma \approx 3$ value in Fig.15 for low reduced temperatures compared to higher ones. This results in a substantial decrease of the coefficient for $V_b : Gu$ at lower reduced temperatures although the vapor boundary is located only 1σ closer to the interphase compared to $V_b : Wolf$. A similar conclusion holds for the coefficients of Meland at low reduced temperatures. Due to rarefied vapor conditions at low temperatures, the determination of the vapor boundary of Meland using the vapor pressure becomes less accurate. Hence, the vapor boundary method is responsible for the anomalous behaviour of the coefficients at low reduced temperatures given the fact that the method of Wolf is able to provide the expected monotonic decay using the liquid boundary method of Gu.

In Fig.17, the log of the quantity δ_0/λ for the transmission expression α_T (Eq.(8)) and the log of the dimensionless capillary wave length scale $\sqrt{k_b T/(\gamma \lambda^2)}$ (54; 55; 56) can be related as shown in the figure. This holds for all monatomic fluids in this study (i.e. Ne,Ar,Kr,Xe) and provides a surprisingly simple approximation for δ_0/λ in terms of measurable parameters.

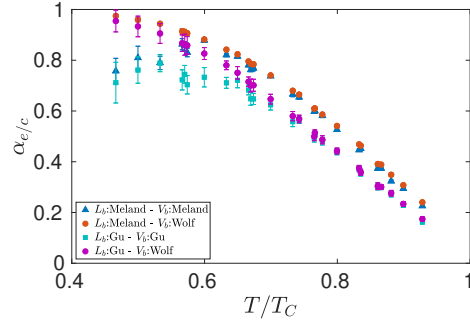


Figure 16: Evaporation/condensation coefficient as function of reduced temperature using the method of Meland, Gu and Wolf.

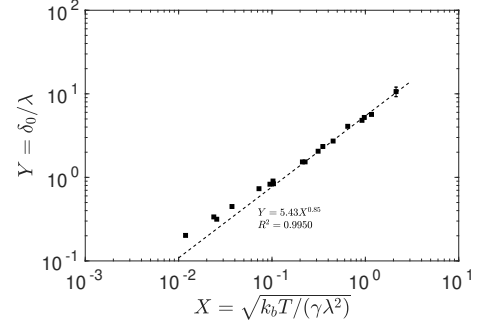


Figure 17: Dimensionless excess length δ_0/λ as function dimensionless capillary wave length scale $\sqrt{k_b T/\gamma\lambda^2}$.

A comparison with Gu(9) and Ishiyama(12) is shown in Fig.18. At low reduced temperatures the coefficients coincide with the results of Ishiyama(12) but start to deviate towards higher reduced temperatures. Coefficients defined by Ishiyama are used in kinetic models which assume that the vapor behaves like an ideal gas. This is a good approximation for the behavior of the vapor at low reduced temperatures. When moving towards higher reduced temperatures, the behaviour of the vapor becomes less ideal. Evaporating particles will exhibit more resistance from the incident particles. It is therefore expected that $\langle J_{evap}^{SP} \rangle$ as defined by Ishiyama will overestimate the evaporating mass flux from equilibrium MD simulations. As a consequence, higher coefficients are predicted at higher reduced temperatures.

The results for Gu deviate at low reduced temperatures and have insignificant difference at higher temperatures. A similar behavior was observed in Fig.16 and discussed above. A low accuracy of the criteria value C_v and a rapid change of the coefficient in the interphase region at low reduced temperatures are responsible to the decrease of the evaporation coefficient. For higher reduced temperatures, the coefficients are less sensitive to the position of the vapor boundary due to the less rapid change of the coefficient in the interphase region. Hence, results of Gu and Wolf converge although the vapor boundary positions differentiate between $1\sigma - 2.5\sigma$.

The transmission probability α_T in Fig.18 is obtained using Eq.(8) and equation $Y = 5.43X^{0.85}$ shown in Fig.17. Here, $X = \sqrt{k_b T/\gamma\lambda^2}$ is dimensionless capillary wave length scale and $Y = \delta_0/\lambda$ excess length. At lower reduced temperatures, this equation underestimates the excess length δ_0 resulting in a higher evaporation/condensation coefficient.

It is concluded that the method of Wolf provides the expected monotonic decay of the evaporation/condensation coefficient for temperatures between its triple and critical point. At low temperatures, it is less sensitive to statistical fluctuations in the vapor phase compared to the methods of Meland and Gu. Thereby avoiding any anomalous behaviour of the coefficients. *It coincides with the accurate results of Ishiyama at low reduced temperatures and Gu at higher reduced temperatures which confirms the robustness and accuracy of the alternative method (Wolf).*

4 Conclusions

First, the transport behavior of argon vapor was discussed by investigating the particle diffusion in pure vapor. Depending on the particle random walk behavior, the probability of particles to diffuse over a distance δ can be quantified by the flux ratio α_{LV} . This ratio as function of δ/λ is well described by a logistic curve. Similarly, the density ratio ρ_D/ρ_v and velocity ratio U_D/U_v maintain the same logistic behavior. For small distance (i.e. $\delta/\lambda \ll 1$), the density ratio equals half the vapor density whereas the velocity ratio is twice the average outgoing velocity U_v . When the distance increases, the density ratio converges to zero and the velocity ratio to approximately 2.55. Transmission probability theory is capable of describing the flux ratio very well by considering particle diffusion at dimensions of the mean free path.

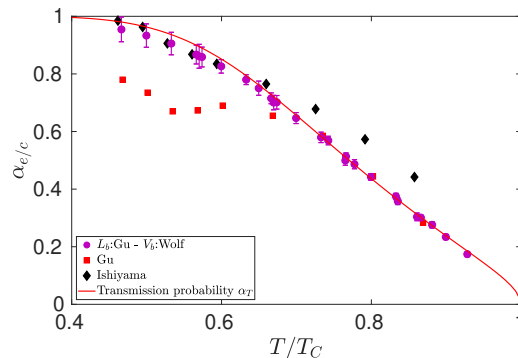


Figure 18: Evaporation/condensation coefficient using $L_b : Gu - V_b : Wolf$ as function of reduced temperature compared to Gu(9), Ishiyama(12) and transmission probability α_T of Eq.(8).

The alternative method (Wolf) for determining the vapor boundary position introduced in this study is based on the behavior of the flux ratio α_{LV} within the interphase region. By scanning the position of the sink boundary in the direction orthogonal to the liquid/vapor interface from the liquid boundary towards the vapor phase, a local maximum of the flux ratio is obtained in the vapor phase. It has been shown that the location of this local maximum represents the transition from the interphase to the vapor phase. It is in close agreement with the start of a constant outgoing mass flux J_{out} as well as the beginning of the linear decay of the evaporating particle density ρ_{evap} which is the expected behavior of the vapor phase. Furthermore, the Kullback-Leibler (KL) divergence quantifies the difference of the velocity distribution of evaporating particles from the Maxwellian velocity distribution. Within the interphase region, the KL-divergence changed three orders of magnitude and changed to a gradual increase afterwards at the location of the local maximum. Finally, Berman's expression of transmission probability theory fitted very well to the results of the flux ratio α_{LV} in the vapor region and showed a rapid deviation when crossing the local maximum. All of these observations and its independency of the liquid boundary position clearly illustrates the significance of the location of the local maximum. It is therefore considered to be the correct physical location of the vapor boundary and defines the beginning of the vapor phase.

The alternative method shares the advantages of the existing methods such as simplicity but eliminate their disadvantages such as additional MD simulations or the use of an equation of state.

Due to the somewhat ad-hoc definition for the liquid boundary of Meland, the current study focussed on applying the alternative method (Wolf) using the liquid boundary obtained by Gu. It is shown in Fig.10 that the best linear fit between the interphase thickness ($z_{V_b} - z_{L_b}$) and w_t (Eq.(2)) is obtained for the combination of $L_b : Gu - V_b : Wolf$ which according to Weeks(53) provide the most accurate definition of the interphase thickness.

All monatomic fluids in the present study have similar evaporation/condensation coefficients as function of the reduced temperature. Despite significant difference in mass and interaction energy between the fluids, it is concluded that the static molecular properties do not play an important role in the evaporation process. The small difference between the results of the flux ratio α_{LV} and evaporation/condensation coefficient $\alpha_{e/c}$ in Fig.13 suggests that the probability of particles to evaporate is mainly influenced by the diffusion behavior in the vapor phase.

At low reduced temperatures, the vapor boundary positions of Meland and Gu become less accurate due to the rarefied vapor conditions. As a consequence, the evaporation/condensation coefficients show anomalous behaviour near low reduced temperatures whereas the alternative method (Wolf) provides a monotonic decay over the entire temperature range. Berman's expression of transmission probability theory gives accurate approximations of the coefficients over a large temperature range.

This is the author's peer reviewed, accepted manuscript. However, the online version of record will be different from this version once it has been copyedited and typeset.

PLEASE CITE THIS ARTICLE AS DOI: 10.1063/1.50213744

The ideal gas assumption made by Ishiyama are only valid at low reduced temperatures. This causes the evaporation mass flux to be overestimated at higher reduced temperatures, hence higher evaporation/condensation coefficients are predicted. As mentioned above, the results of Gu are less accurate at low reduced temperatures because of the large statistical fluctuations in the vapor phase. The alternative method (Wolf) coincides with the accurate results of Ishiyama at low reduced temperatures and Gu and higher reduced temperatures which confirms its robustness and accuracy.

Finally, the alternative method has been applied to non-equilibrium simulations(57; 58) and its evaporation and condensation coefficients used as input for the S-model kinetic equation(5). The results show good agreement for vapor density, pressure, temperature, evaporation velocity and heat flux. This confirms that the alternative method is suited for extracting the evaporation/condensation coefficient but moreover provides the correct coefficient to be used in kinetic models such as S-model kinetic equation.

Acknowledgements

This project has received funding from the European Union's Horizon 2020 research and innovation programme under the Marie Skłodowska-Curie grant agreement No. 643095.

Conflict of Interest Statement

The author (authors) has (have) no conflicts to disclose.

Data Availability Statement

The data that support the findings of this study are available within the article.

A Fluid properties

A.1 Neon

Notation: first value is the mean value followed by its standard deviation.

Table 2: Neon liquid-vapor equilibrium properties

T/T_C	T	ρ_v	ρ_l	P_V	ΔH	C_l	C_v	d/σ	$\lambda(38)$
	K	kg/m^3	kg/m^3	$10^6 N/m^2$	kJ/kg			(Eq.(2))	\AA
0.65	27.94 ± 0.27	11.79 ± 0.27	1199.15 ± 1.51	$0.13 \pm 0.00^*$	89.41 ± 0.72	2.87 ± 0.01	$0.04 \pm 0.00^*$	2.38 ± 0.04	42.84
0.74	32.00 ± 0.15	31.40 ± 0.41	1112.61 ± 1.74	0.36 ± 0.01	81.10 ± 0.55	2.66 ± 0.01	$0.10 \pm 0.00^*$	3.04 ± 0.06	17.88
0.84	35.99 ± 0.12	71.74 ± 0.75	1009.29 ± 2.34	0.81 ± 0.02	69.14 ± 0.54	2.40 ± 0.01	$0.22 \pm 0.00^*$	4.19 ± 0.10	8.89
0.93	40.05 ± 0.10	155.84 ± 1.26	866.23 ± 3.57	1.58 ± 0.04	50.59 ± 0.56	2.07 ± 0.01	0.46 ± 0.01	7.15 ± 0.19	4.93

* standard deviation is less than 0.005

Table 3: Neon liquid-vapor boundary properties using the method of **Meland** for the **liquid boundary**

L_b : Meland	V_b : Wolf					V_b : Meland				V_b : Gu			
T/T_C	z_{L_b}/σ	z_{V_b}/σ	\bar{d}^{**}/σ	α_e	α_c	z_{V_b}/σ	\bar{d}^{**}/σ	α_e	α_c	z_{V_b}/σ	\bar{d}^{**}/σ	α_e	α_c
0.65	-1.20 ± 0.01	3.52 ± 0.18	4.71 ± 0.18	0.82 ± 0.01	0.82 ± 0.01	3.32 ± 0.18	4.52 ± 0.18	0.82 ± 0.01	0.82 ± 0.01	3.21 ± 0.05	4.41 ± 0.05	0.82 ± 0.01	0.82 ± 0.01
0.74	-1.53 ± 0.01	3.83 ± 0.29	5.36 ± 0.29	0.66 ± 0.01	0.66 ± 0.01	3.57 ± 0.14	5.10 ± 0.14	0.65 ± 0.01	0.65 ± 0.01	3.92 ± 0.08	5.45 ± 0.08	0.66 ± 0.01	0.66 ± 0.01
0.84	-2.10 ± 0.02	4.35 ± 0.37	6.44 ± 0.36	$0.46 \pm 0.00^*$	0.46 ± 0.01	3.77 ± 0.06	5.87 ± 0.06	0.45 ± 0.01	0.45 ± 0.01	4.90 ± 0.13	7.00 ± 0.13	$0.46 \pm 0.00^*$	$0.46 \pm 0.00^*$
0.93	-3.58 ± 0.07	5.20 ± 0.49	8.76 ± 0.56	$0.24 \pm 0.00^*$	$0.24 \pm 0.00^*$	3.49 ± 0.07	7.07 ± 0.10	$0.23 \pm 0.00^*$	$0.23 \pm 0.00^*$	7.19 ± 0.12	10.77 ± 0.16	$0.23 \pm 0.00^*$	$0.23 \pm 0.00^*$

* standard deviation is less than 0.005

** \bar{d} is the time-averaged interphase thickness, i.e. $\overline{z_{V_b} - z_{L_b}}$

Table 4: Neon liquid-vapor boundary properties using the method of **Gu** for the **liquid boundary**

L_b : Gu	V_b : Wolf					V_b : Meland				V_b : Gu			
T/T_C	z_{L_b}/σ	z_{V_b}/σ	\bar{d}^{**}/σ	α_e	α_c	z_{V_b}/σ	\bar{d}^{**}/σ	α_e	α_c	z_{V_b}/σ	\bar{d}^{**}/σ	α_e	α_c
0.65	-3.14 ± 0.03	3.62 ± 0.19	6.76 ± 0.20	0.75 ± 0.02	0.75 ± 0.02	3.32 ± 0.18	6.45 ± 0.18	0.74 ± 0.02	0.74 ± 0.02	3.21 ± 0.05	6.35 ± 0.07	0.74 ± 0.02	0.74 ± 0.02
0.74	-3.64 ± 0.03	3.96 ± 0.31	7.60 ± 0.31	0.57 ± 0.01	0.57 ± 0.01	3.57 ± 0.14	7.21 ± 0.15	0.56 ± 0.01	0.56 ± 0.01	3.92 ± 0.08	7.56 ± 0.11	0.57 ± 0.01	0.57 ± 0.01
0.84	-4.45 ± 0.07	4.68 ± 0.39	9.13 ± 0.42	0.38 ± 0.01	0.38 ± 0.01	3.77 ± 0.06	8.22 ± 0.09	0.36 ± 0.01	0.36 ± 0.01	4.90 ± 0.13	9.35 ± 0.18	0.37 ± 0.01	0.37 ± 0.01
0.93	-6.32 ± 0.16	5.92 ± 0.49	12.24 ± 0.54	0.19 ± 0.01	0.19 ± 0.01	3.49 ± 0.07	9.81 ± 0.16	$0.18 \pm 0.00^*$	$0.18 \pm 0.00^*$	7.19 ± 0.12	13.51 ± 0.25	$0.19 \pm 0.00^*$	$0.19 \pm 0.00^*$

* standard deviation is less than 0.005

** \bar{d} is the time-averaged interphase thickness, i.e. $\overline{z_{V_b} - z_{L_b}}$

This is the author's peer reviewed, accepted manuscript. However, the online version of record will be different from this version once it has been copyedited and typeset.

PLEASE CITE THIS ARTICLE AS DOI: 10.1063/1.50213744

A.2 Argon

Notation: first value is the mean value followed by its standard deviation.

Table 5: Argon liquid-vapor equilibrium properties

T/T_C	T K	ρ_v kg/m^3	ρ_l kg/m^3	P_V $10^6 N/m^2$	ΔH kJ/kg	C_l	C_v	d/σ (Eq.(2))	$\lambda(38)$ \AA
0.47	69.41 ± 2.54	0.60 ± 0.05	1498.43 ± 1.20	0.011 ± 0.001	176.21 ± 2.98	3.21 ± 0.010	0.002 ± 0.004	1.63 ± 0.03	935.67
0.50	74.97 ± 2.20	1.28 ± 0.07	1471.07 ± 1.25	0.021 ± 0.002	173.60 ± 2.45	3.15 ± 0.009	0.004 ± 0.004	1.76 ± 0.02	456.27
0.53	80.00 ± 2.41	2.50 ± 0.18	1440.88 ± 1.90	0.044 ± 0.004	170.08 ± 2.98	3.09 ± 0.009	0.008 ± 0.006	1.83 ± 0.04	241.86
0.57	84.99 ± 1.96	4.40 ± 0.22	1411.31 ± 2.01	0.08 ± 0.01	166.58 ± 2.42	3.03 ± 0.01	0.01 ± 0.01	1.93 ± 0.02	142.31
0.60	90.02 ± 1.53	7.23 ± 0.31	1380.60 ± 2.06	0.13 ± 0.01	162.55 ± 1.98	2.96 ± 0.01	0.02 ± 0.01	2.10 ± 0.03	89.76
0.63	95.14 ± 1.30	11.22 ± 0.38	1349.16 ± 2.19	0.21 ± 0.01	158.53 ± 1.78	2.90 ± 0.01	0.03 ± 0.01	2.26 ± 0.04	59.88
0.67	99.72 ± 1.03	16.74 ± 0.44	1316.00 ± 2.35	0.32 ± 0.01	153.35 ± 1.52	2.82 ± 0.01	0.05 ± 0.01	2.47 ± 0.03	41.66
0.70	105.02 ± 0.95	23.82 ± 0.57	1281.94 ± 2.46	0.47 ± 0.02	148.58 ± 1.51	2.75 ± 0.01	0.07 ± 0.01	2.68 ± 0.05	30.27
0.73	110.04 ± 0.80	33.21 ± 0.70	1246.01 ± 2.68	0.67 ± 0.02	142.89 ± 1.36	2.67 ± 0.01	0.09 ± 0.01	2.96 ± 0.07	22.66
0.77	114.87 ± 0.71	45.46 ± 0.81	1207.54 ± 2.82	0.91 ± 0.03	136.16 ± 1.34	2.59 ± 0.01	0.13 ± 0.01	3.26 ± 0.06	17.25
0.80	120.07 ± 0.65	61.08 ± 1.12	1166.54 ± 3.22	1.23 ± 0.04	129.13 ± 1.36	2.50 ± 0.01	0.17 ± 0.01	3.63 ± 0.06	13.44
0.83	125.24 ± 0.57	80.42 ± 1.25	1121.55 ± 3.61	1.61 ± 0.05	120.98 ± 1.34	2.40 ± 0.01	0.22 ± 0.01	4.11 ± 0.07	10.75
0.87	129.99 ± 0.52	106.84 ± 1.50	1071.49 ± 4.05	2.07 ± 0.06	110.62 ± 1.32	2.29 ± 0.01	0.29 ± 0.01	4.77 ± 0.11	8.53
0.90	134.95 ± 0.51	141.22 ± 2.33	1013.85 ± 4.56	2.62 ± 0.08	98.64 ± 1.44	2.17 ± 0.02	0.37 ± 0.01	5.76 ± 0.09	6.94

This is the author's peer reviewed, accepted manuscript. However, the online version of record will be different from this version once it has been copyedited and typeset.

PLEASE CITE THIS ARTICLE AS DOI: 10.1063/1.50213744

Table 6: Argon liquid-vapor boundary properties using the method of Meland for the liquid boundary

L_b : Meland	V_b : Wolf					V_b : Meland				V_b : Gu			
	T/T_C	z_L/σ	z_V/σ	\bar{d}^{**}/σ	α_c	α_c	z_V/σ	\bar{d}^{**}/σ	α_c	α_c	z_V/σ	\bar{d}^{**}/σ	α_c
0.47	-0.82 ± 0.00*	3.46 ± 0.62	4.38 ± 0.60	0.97 ± 0.01	0.98 ± 0.01	2.17 ± 0.09	2.99 ± 0.09	0.76 ± 0.05	0.76 ± 0.04	2.11 ± 0.10	2.93 ± 0.10	0.74 ± 0.06	0.75 ± 0.05
0.50	-0.89 ± 0.01	3.46 ± 0.44	4.35 ± 0.35	0.96 ± 0.01	0.96 ± 0.01	2.47 ± 0.08	3.35 ± 0.08	0.81 ± 0.05	0.81 ± 0.05	2.38 ± 0.15	3.27 ± 0.15	0.80 ± 0.04	0.80 ± 0.05
0.53	-0.92 ± 0.04	3.43 ± 0.64	4.36 ± 0.45	0.94 ± 0.01	0.94 ± 0.01	2.32 ± 0.11	3.24 ± 0.11	0.79 ± 0.03	0.79 ± 0.03	2.38 ± 0.10	3.30 ± 0.09	0.84 ± 0.02	0.83 ± 0.02
0.57	-0.97 ± 0.01	3.30 ± 0.38	4.29 ± 0.33	0.91 ± 0.01	0.91 ± 0.01	3.23 ± 0.75	4.21 ± 0.74	0.86 ± 0.02	0.86 ± 0.03	2.38 ± 0.03	3.35 ± 0.04	0.81 ± 0.02	0.81 ± 0.02
0.60	-1.06 ± 0.00*	3.34 ± 0.28	4.42 ± 0.25	0.88 ± 0.01	0.88 ± 0.01	3.19 ± 0.12	4.25 ± 0.12	0.88 ± 0.01	0.88 ± 0.01	2.61 ± 0.03	3.67 ± 0.03	0.83 ± 0.01	0.83 ± 0.01
0.63	-1.14 ± 0.01	3.49 ± 0.21	4.61 ± 0.21	0.84 ± 0.00*	0.84 ± 0.00*	3.03 ± 0.16	4.16 ± 0.15	0.82 ± 0.01	0.82 ± 0.01	2.89 ± 0.05	4.03 ± 0.05	0.81 ± 0.01	0.81 ± 0.01
0.67	-1.24 ± 0.01	3.48 ± 0.22	4.73 ± 0.22	0.80 ± 0.01	0.80 ± 0.01	3.10 ± 0.03	4.35 ± 0.02	0.78 ± 0.01	0.78 ± 0.01	3.23 ± 0.05	4.47 ± 0.05	0.79 ± 0.01	0.79 ± 0.01
0.70	-1.34 ± 0.01	3.61 ± 0.15	4.95 ± 0.15	0.74 ± 0.01	0.74 ± 0.00*	3.53 ± 0.08	4.88 ± 0.08	0.74 ± 0.00*	0.74 ± 0.01	3.44 ± 0.06	4.78 ± 0.06	0.74 ± 0.01	0.74 ± 0.01
0.73	-1.48 ± 0.01	3.74 ± 0.24	5.20 ± 0.24	0.68 ± 0.01	0.68 ± 0.01	3.31 ± 0.13	4.79 ± 0.13	0.67 ± 0.01	0.67 ± 0.01	3.70 ± 0.08	5.18 ± 0.07	0.68 ± 0.01	0.68 ± 0.01
0.77	-1.64 ± 0.01	3.90 ± 0.23	5.54 ± 0.23	0.61 ± 0.00*	0.61 ± 0.00*	3.49 ± 0.06	5.13 ± 0.06	0.60 ± 0.01	0.60 ± 0.01	3.96 ± 0.07	5.60 ± 0.07	0.61 ± 0.01	0.61 ± 0.01
0.80	-1.81 ± 0.02	4.07 ± 0.20	5.89 ± 0.20	0.54 ± 0.00*	0.54 ± 0.01	3.46 ± 0.09	5.27 ± 0.08	0.53 ± 0.01	0.53 ± 0.01	4.28 ± 0.07	6.10 ± 0.08	0.54 ± 0.00*	0.54 ± 0.00*
0.83	-2.05 ± 0.02	4.19 ± 0.35	6.25 ± 0.35	0.47 ± 0.00*	0.47 ± 0.00*	3.36 ± 0.12	5.41 ± 0.11	0.45 ± 0.00*	0.45 ± 0.00*	4.70 ± 0.10	6.76 ± 0.10	0.46 ± 0.00*	0.46 ± 0.00*
0.87	-2.39 ± 0.04	4.54 ± 0.29	6.93 ± 0.29	0.39 ± 0.00*	0.39 ± 0.00*	3.57 ± 0.06	5.96 ± 0.03	0.37 ± 0.00*	0.37 ± 0.01	5.16 ± 0.15	7.55 ± 0.17	0.38 ± 0.00*	0.38 ± 0.00*
0.90	-2.89 ± 0.02	4.81 ± 0.42	7.68 ± 0.41	0.31 ± 0.00*	0.31 ± 0.00*	3.67 ± 0.10	6.55 ± 0.09	0.30 ± 0.00*	0.30 ± 0.00*	5.91 ± 0.08	8.80 ± 0.08	0.30 ± 0.00*	0.30 ± 0.00*

* standard deviation is less than 0.005

** \bar{d} is the time-averaged interphase thickness, i.e. $(z_V - z_L)$

This is the author's peer reviewed, accepted manuscript. However, the online version of record will be different from this version once it has been copyedited and typeset.

PLEASE CITE THIS ARTICLE AS DOI: 10.1063/1.50213744

Table 7: Argon liquid-vapor boundary properties using the method of **Gu** for the **liquid boundary**

L_b : Gu	V_b : Wolf					V_b : Meland				V_b : Gu			
	T/T_C	z_L/σ	z_V/σ	\bar{d}^{**}/σ	α_e	α_c	z_V/σ	\bar{d}^{**}/σ	α_e	α_c	z_V/σ	\bar{d}^{**}/σ	α_e
0.47	-2.34 ± 0.23	3.37 ± 0.79	5.84 ± 0.75	0.95 ± 0.04	0.97 ± 0.05	2.17 ± 0.09	4.51 ± 0.21	0.73 ± 0.07	0.74 ± 0.07	2.11 ± 0.10	4.44 ± 0.27	0.71 ± 0.08	0.73 ± 0.08
	0.53	-2.62 ± 0.09	3.43 ± 0.51	6.15 ± 0.37	0.93 ± 0.04	0.94 ± 0.05	2.47 ± 0.08	5.08 ± 0.17	0.77 ± 0.05	0.78 ± 0.06	2.38 ± 0.15	5.00 ± 0.16	0.76 ± 0.05
0.53	-2.84 ± 0.20	3.39 ± 0.52	6.27 ± 0.55	0.91 ± 0.04	0.91 ± 0.04	2.32 ± 0.11	5.17 ± 0.18	0.74 ± 0.04	0.74 ± 0.05	2.38 ± 0.10	5.22 ± 0.24	0.79 ± 0.03	0.79 ± 0.05
	0.57	-2.70 ± 0.02	3.28 ± 0.39	6.02 ± 0.28	0.87 ± 0.03	0.87 ± 0.03	3.23 ± 0.75	5.93 ± 0.77	0.82 ± 0.03	0.82 ± 0.04	2.38 ± 0.03	5.08 ± 0.04	0.75 ± 0.03
0.60	-2.83 ± 0.03	3.37 ± 0.30	6.23 ± 0.25	0.83 ± 0.02	0.83 ± 0.03	3.19 ± 0.12	6.02 ± 0.12	0.82 ± 0.02	0.82 ± 0.03	2.61 ± 0.03	5.44 ± 0.06	0.77 ± 0.02	0.77 ± 0.02
	0.63	-2.96 ± 0.04	3.58 ± 0.23	6.51 ± 0.24	0.78 ± 0.02	0.78 ± 0.02	3.03 ± 0.16	5.98 ± 0.14	0.75 ± 0.01	0.75 ± 0.02	2.89 ± 0.05	5.85 ± 0.08	0.75 ± 0.02
0.67	-3.10 ± 0.05	3.58 ± 0.21	6.69 ± 0.20	0.72 ± 0.02	0.72 ± 0.02	3.10 ± 0.03	6.20 ± 0.03	0.70 ± 0.02	0.70 ± 0.02	3.23 ± 0.05	6.32 ± 0.08	0.71 ± 0.02	0.71 ± 0.02
	0.70	-3.26 ± 0.04	3.73 ± 0.22	6.99 ± 0.22	0.66 ± 0.02	0.66 ± 0.01	3.53 ± 0.08	6.80 ± 0.09	0.65 ± 0.01	0.65 ± 0.01	3.44 ± 0.06	6.70 ± 0.09	0.65 ± 0.01
0.73	-3.46 ± 0.04	3.87 ± 0.24	7.33 ± 0.26	0.59 ± 0.01	0.59 ± 0.01	3.31 ± 0.13	6.77 ± 0.15	0.57 ± 0.01	0.57 ± 0.01	3.70 ± 0.08	7.16 ± 0.11	0.59 ± 0.01	0.59 ± 0.01
	0.77	-3.66 ± 0.06	4.12 ± 0.22	7.78 ± 0.24	0.52 ± 0.01	0.52 ± 0.01	3.49 ± 0.06	7.14 ± 0.07	0.51 ± 0.01	0.51 ± 0.01	3.96 ± 0.07	7.62 ± 0.11	0.52 ± 0.01
0.80	-3.92 ± 0.06	4.32 ± 0.21	8.24 ± 0.23	0.45 ± 0.01	0.45 ± 0.01	3.46 ± 0.09	7.38 ± 0.10	0.43 ± 0.01	0.43 ± 0.01	4.28 ± 0.07	8.20 ± 0.11	0.45 ± 0.01	0.45 ± 0.01
	0.83	-4.23 ± 0.07	4.48 ± 0.35	8.73 ± 0.34	0.39 ± 0.01	0.39 ± 0.01	3.36 ± 0.12	7.59 ± 0.14	0.36 ± 0.01	0.36 ± 0.01	4.70 ± 0.10	8.93 ± 0.14	0.38 ± 0.01
0.87	-4.64 ± 0.09	4.87 ± 0.31	9.51 ± 0.31	0.32 ± 0.01	0.32 ± 0.01	3.57 ± 0.06	8.21 ± 0.09	0.30 ± 0.01	0.30 ± 0.01	5.16 ± 0.15	9.80 ± 0.19	0.32 ± 0.01	0.32 ± 0.01
	0.90	-5.22 ± 0.06	5.25 ± 0.44	10.47 ± 0.44	0.25 ± 0.00*	0.25 ± 0.00*	3.67 ± 0.10	8.88 ± 0.11	0.23 ± 0.00*	0.23 ± 0.00*	5.91 ± 0.08	11.13 ± 0.11	0.25 ± 0.00*

* standard deviation is less than 0.005

** \bar{d} is the time-averaged interphase thickness, i.e. $\overline{z_V - z_{L_b}}$

This is the author's peer reviewed, accepted manuscript. However, the online version of record will be different from this version once it has been copyedited and typeset.

PLEASE CITE THIS ARTICLE AS DOI: 10.1063/5.0213744

A.3 Krypton

Notation: first value is the mean value followed by its standard deviation.

Table 8: Krypton liquid-vapor equilibrium properties

T/T_C	T	ρ_v	ρ_l	P_V	ΔH	C_l	C_v	d/σ	$\lambda(38)$
	K	kg/m^3	kg/m^3	$10^6 N/m^2$	kJ/kg			(Eq.(2))	\AA
0.57	119.78 ± 2.61	8.80 ± 0.45	2412.32 ± 3.93	0.10 ± 0.01	109.48 ± 1.60	3.01 ± 0.01	0.02 ± 0.01	1.96 ± 0.04	132.03
0.67	139.67 ± 1.55	30.81 ± 0.89	2254.05 ± 4.55	0.39 ± 0.02	100.98 ± 1.13	2.81 ± 0.01	0.05 ± 0.01	2.48 ± 0.05	41.85
0.77	160.09 ± 1.18	79.07 ± 1.65	2073.78 ± 5.52	1.06 ± 0.04	90.13 ± 1.04	2.58 ± 0.01	0.13 ± 0.01	3.23 ± 0.07	18.27
0.86	179.90 ± 0.85	179.71 ± 2.92	1850.50 ± 7.35	2.31 ± 0.08	73.83 ± 0.97	2.30 ± 0.01	0.28 ± 0.01	4.68 ± 0.11	9.29

Table 9: Krypton liquid-vapor boundary properties using the method of Meland for the liquid boundary

L_b : Meland	V_b : Wolf					V_b : Meland				V_b : Gu			
T/T_C	z_L/σ	z_V/σ	\bar{d}^{**}/σ	α_e	α_c	z_V/σ	\bar{d}^{**}/σ	α_e	α_c	z_V/σ	\bar{d}^{**}/σ	α_e	α_c
0.57	-0.99 ± 0.01	3.31 ± 0.39	4.31 ± 0.38	0.91 ± 0.01	0.91 ± 0.01	2.52 ± 0.05	3.51 ± 0.05	0.83 ± 0.02	0.83 ± 0.02	2.38 ± 0.05	3.37 ± 0.05	0.80 ± 0.01	0.80 ± 0.01
0.67	-1.25 ± 0.01	3.49 ± 0.29	4.73 ± 0.30	0.79 ± 0.01	0.79 ± 0.01	3.07 ± 0.08	4.32 ± 0.09	0.76 ± 0.01	0.76 ± 0.01	3.20 ± 0.06	4.44 ± 0.06	0.77 ± 0.01	0.77 ± 0.01
0.77	-1.62 ± 0.02	3.82 ± 0.32	5.45 ± 0.32	0.61 ± 0.01	0.61 ± 0.01	3.35 ± 0.18	4.98 ± 0.18	0.60 ± 0.01	0.60 ± 0.01	3.91 ± 0.07	5.53 ± 0.07	0.61 ± 0.00*	0.61 ± 0.01
0.86	-2.34 ± 0.04	4.52 ± 0.38	6.86 ± 0.36	0.39 ± 0.01	0.39 ± 0.01	3.74 ± 0.42	6.08 ± 0.43	0.37 ± 0.01	0.37 ± 0.01	5.07 ± 0.13	7.41 ± 0.13	0.39 ± 0.00*	0.39 ± 0.01

* standard deviation is less than 0.005

** \bar{d} is the time-averaged interphase thickness, i.e. $\overline{z_{V_i} - z_{L_b}}$

Table 10: Krypton liquid-vapor boundary properties using the method of Gu for the liquid boundary

L_b : Gu	V_b : Wolf					V_b : Meland				V_b : Gu			
T/T_C	z_L/σ	z_V/σ	\bar{d}^{**}/σ	α_e	α_c	z_V/σ	\bar{d}^{**}/σ	α_e	α_c	z_V/σ	\bar{d}^{**}/σ	α_e	α_c
0.57	-2.70 ± 0.03	3.33 ± 0.39	6.05 ± 0.36	0.86 ± 0.03	0.86 ± 0.03	2.52 ± 0.05	5.22 ± 0.07	0.78 ± 0.03	0.78 ± 0.03	2.38 ± 0.05	5.08 ± 0.07	0.75 ± 0.02	0.75 ± 0.02
0.67	-3.09 ± 0.04	3.58 ± 0.34	6.67 ± 0.33	0.71 ± 0.02	0.71 ± 0.02	3.07 ± 0.08	6.16 ± 0.09	0.68 ± 0.02	0.68 ± 0.02	3.20 ± 0.06	6.29 ± 0.09	0.70 ± 0.02	0.70 ± 0.02
0.77	-3.60 ± 0.06	4.01 ± 0.26	7.60 ± 0.28	0.52 ± 0.01	0.52 ± 0.01	3.35 ± 0.18	6.95 ± 0.20	0.50 ± 0.01	0.50 ± 0.01	3.91 ± 0.07	7.50 ± 0.11	0.52 ± 0.01	0.52 ± 0.01
0.86	-4.50 ± 0.08	4.95 ± 0.39	9.44 ± 0.40	0.32 ± 0.01	0.32 ± 0.01	3.74 ± 0.42	8.24 ± 0.42	0.30 ± 0.01	0.30 ± 0.01	5.07 ± 0.13	9.57 ± 0.17	0.32 ± 0.01	0.32 ± 0.01

** \bar{d} is the time-averaged interphase thickness, i.e. $\overline{z_{V_i} - z_{L_b}}$

This is the author's peer reviewed, accepted manuscript. However, the online version of record will be different from this version once it has been copyedited and typeset.

PLEASE CITE THIS ARTICLE AS DOI: 10.1063/5.0213744

A.4 Xenon

Notation: first value is the mean value followed by its standard deviation.

Table 11: Xenon liquid-vapor equilibrium properties

T/T_C	T	ρ_v	ρ_l	P_V	ΔH	C_l	C_v	d/σ	$\lambda(38)$
	K	kg/m^3	kg/m^3	$10^6 N/m^2$	kJ/kg			(Eq.(2))	\AA
0.57	165.27 ± 4.32	10.02 ± 0.60	2936.28 ± 5.46	0.10 ± 0.01	97.43 ± 1.68	3.02 ± 0.01	0.01 ± 0.01	1.92 ± 0.03	152.42
0.67	195.01 ± 2.34	37.48 ± 1.29	2729.54 ± 6.45	0.43 ± 0.02	89.54 ± 1.15	2.81 ± 0.01	0.05 ± 0.01	2.45 ± 0.04	45.52
0.78	224.54 ± 1.72	104.55 ± 2.54	2490.48 ± 7.92	1.23 ± 0.05	78.49 ± 1.04	2.55 ± 0.01	0.14 ± 0.01	3.31 ± 0.05	18.49
0.88	255.26 ± 1.28	253.52 ± 3.81	2181.53 ± 11.47	2.84 ± 0.11	61.89 ± 1.00	2.24 ± 0.02	0.32 ± 0.01	5.13 ± 0.06	9.01

Table 12: Xenon liquid-vapor boundary properties using the method of Meland for the liquid boundary

L_b : Meland	V_b : Wolf					V_b : Meland				V_b : Gu			
T/T_C	z_L/σ	z_V/σ	\bar{d}^{**}/σ	α_e	α_c	z_V/σ	\bar{d}^{**}/σ	α_e	α_c	z_V/σ	\bar{d}^{**}/σ	α_e	α_c
0.57	$-0.96 \pm 0.00^*$	3.32 ± 0.44	4.31 ± 0.41	0.91 ± 0.01	0.91 ± 0.01	$2.60 \pm 0.00^*$	$3.56 \pm 0.00^*$	0.86 ± 0.02	0.86 ± 0.02	2.28 ± 0.03	3.24 ± 0.04	0.78 ± 0.02	0.78 ± 0.02
0.67	-1.23 ± 0.01	3.45 ± 0.23	4.68 ± 0.23	0.78 ± 0.01	0.78 ± 0.01	3.23 ± 0.15	4.46 ± 0.15	0.77 ± 0.01	0.77 ± 0.01	3.08 ± 0.05	4.32 ± 0.05	0.77 ± 0.01	0.77 ± 0.01
0.78	-1.66 ± 0.02	3.87 ± 0.33	5.53 ± 0.32	0.59 ± 0.01	0.59 ± 0.01	3.57 ± 0.41	5.23 ± 0.41	0.58 ± 0.01	0.58 ± 0.01	3.90 ± 0.08	5.55 ± 0.09	0.58 ± 0.01	0.58 ± 0.01
0.88	-2.58 ± 0.03	4.58 ± 0.33	7.16 ± 0.32	$0.35 \pm 0.00^*$	$0.35 \pm 0.00^*$	3.31 ± 0.08	5.89 ± 0.10	$0.32 \pm 0.00^*$	0.32 ± 0.01	5.29 ± 0.10	7.87 ± 0.11	$0.34 \pm 0.00^*$	$0.34 \pm 0.00^*$

* standard deviation is less than 0.005

** \bar{d} is the time-averaged interphase thickness, i.e. $\overline{z_{V_i} - z_{L_i}}$

Table 13: Xenon liquid-vapor boundary properties using the method of Gu for the liquid boundary

L_b : Gu	V_b : Wolf					V_b : Meland				V_b : Gu			
T/T_C	z_L/σ	z_V/σ	\bar{d}^{**}/σ	α_e	α_c	z_V/σ	\bar{d}^{**}/σ	α_e	α_c	z_V/σ	\bar{d}^{**}/σ	α_e	α_c
0.57	-2.63 ± 0.02	3.40 ± 0.38	6.03 ± 0.34	0.87 ± 0.04	0.87 ± 0.04	$2.60 \pm 0.00^*$	5.22 ± 0.02	0.81 ± 0.03	0.81 ± 0.04	2.28 ± 0.03	4.91 ± 0.05	0.72 ± 0.03	0.72 ± 0.03
0.67	-3.03 ± 0.03	3.55 ± 0.25	6.57 ± 0.24	0.71 ± 0.02	0.71 ± 0.02	3.23 ± 0.15	6.25 ± 0.16	0.69 ± 0.02	0.69 ± 0.02	3.08 ± 0.05	6.11 ± 0.07	0.69 ± 0.02	0.69 ± 0.02
0.78	-3.56 ± 0.05	4.05 ± 0.31	7.63 ± 0.32	0.50 ± 0.01	0.50 ± 0.01	3.57 ± 0.41	7.14 ± 0.40	0.49 ± 0.01	0.49 ± 0.01	3.90 ± 0.08	7.46 ± 0.10	0.50 ± 0.01	0.50 ± 0.01
0.88	-4.72 ± 0.08	4.95 ± 0.27	9.67 ± 0.32	0.28 ± 0.01	0.28 ± 0.01	3.31 ± 0.08	8.03 ± 0.09	0.26 ± 0.01	0.26 ± 0.01	5.29 ± 0.10	10.01 ± 0.09	0.28 ± 0.01	0.28 ± 0.01

* standard deviation is less than 0.005

** \bar{d} is the time-averaged interphase thickness, i.e. $\overline{z_{V_i} - z_{L_i}}$

This is the author's peer reviewed, accepted manuscript. However, the online version of record will be different from this version once it has been copyedited and typeset.

PLEASE CITE THIS ARTICLE AS DOI: 10.1063/1.50213744

References

- [1] A.H. Persad and C.A. Ward. Expressions for the evaporation and condensation coefficients in the hertz-knudsen relation. *Chemical Reviews*, 116:7727–7767, 2016. doi:10.1021/acs.chemrev.5b00511.
- [2] T. Tsuruta, H. Tanaka, and T. Masuoka. Condensation/evaporation coefficient and velocity distributions at liquid–vapor interface. *Int. J. Heat and Mass Transfer*, 42:4107–4116, 1999. doi:10.1016/S0017-9310(99)00081-2.
- [3] Z. Liang, A. Chandra, E. Bird, and P. Keblinski. A molecular dynamics study of transient evaporation and condensation. *International Journal of Heat and Mass Transfer*, 149:9, 2020. doi:https://doi.org/10.1016/j.ijheatmasstransfer.2019.119152.
- [4] P.L. Bhatnagar, E.P. Gross, and M. Krook. A model for collision processes in gases. i. small amplitude processes in charged and neutral one-component systems. *Physical Review*, 94:511–525, 1954. doi:10.1103/PhysRev.94.511.
- [5] I.A. Graur and A. Polikarpov. Comparison of different kinetic models for the heat transfer problem. *J. Heat and Mass Transfer*, 46:237–244, 2009. doi:10.1007/s00231-009-0558-x.
- [6] E.M. Shakhov. Generalization of the krook kinetic relaxation equation. *Fluid Dynamics*, 3:95–96, 1968. doi:10.1007/BF01029546.
- [7] F.J. Alexander and A.L. Garcia. The direct simulation monte carlo method. *Computers in Physics*, 11:588, 1997. doi:10.1063/1.168619.
- [8] G.A. Bird. *Molecular Gas Dynamics and the Direct Simulation of Gas Flows*. Clarendon Press, Oxford, 1994.
- [9] K. Gu, C.B. Watkins, and J. Koplik. Molecular dynamics simulation of the equilibrium liquid–vapor interphase with solidification. *Fluid Phase Equilibria*, 297(1):77–89, 2010. doi:10.1016/j.fluid.2010.06.014.
- [10] K. Kobayashi, K. Hori, M. Kon, K. Sasaki, and M. Watanabe. Molecular dynamics study on evaporation and reflection of monatomic molecules to construct kinetic boundary condition in vapor–liquid equilibria. *Heat and Mass Transfer*, 52(9):1851, 2015. doi:10.1007/s00231-015-1700-6.
- [11] R. Meland, A. Frezzotti, T. Yttrhus, and B. Hafskjold. Nonequilibrium molecular-dynamics simulation of net evaporation and net condensation, and evaluation of the gas-kinetic boundary condition at the interphase. *Physics of Fluids*, 16(2):223–243, 2004. doi:10.1063/1.1630797.
- [12] T. Ishiyama, T. Yano, and S. Fujikawa. Molecular dynamics study of kinetic boundary condition at an interface between argon vapor and its condensed phase. *Physics of Fluids*, 16:2899, 2004. doi:10.1063/1.1763936.
- [13] M. Matsumoto. Molecular dynamics of fluid phase change. *Fluid Phase Equilibria*, 144:307–314, 1998. doi:10.1016/S0378-3812(97)00274-4.
- [14] G. Nagayama and T. Tsuruta. A general expression for the condensation coefficient based on transition state theory and molecular dynamics simulation. *J. Chemical Physics*, 118:1392–1399, 2003. doi:10.1063/1.1528192.
- [15] T. Tsuruta and G. Nagayama. A molecular dynamics approach to interphase mass transfer between liquid and vapor. *Microscale Thermophysical Engineering*, 6:267–285, 2002. doi:10.1080/10893950290098322.
- [16] M.C.W. Wolf, A. Polikarpov, A.J.H. Frijns, I. Graur, S.V. Nedeia, and R. Enright. Comparison of numerical results of molecular dynamics simulations and s-model kinetic equations for evaporation and condensation of argon. In *Proceedings of the 3rd European Conference on Non-equilibrium Gas Flows*, pages 275–278, 2018.
- [17] M.C.W. Wolf, R. Enright, A.J.H. Frijns, S.V. Nedeia, I. Graur, and A. Polikarpov. The position of the liquid and vapor boundaries and its influence on the evaporation-condensation coefficients. In *Proceedings of the 3rd MIGRATE International Workshop*, pages 56–59, 2018.
- [18] J.S. Rowlinson and B. Widom. *Molecular Theory of Capillarity*. Clarendon Press, Oxford, 1982.
- [19] Giorgio Soave. Equilibrium constants from a modified redlich-kwong equation of state. *Chemical Engineering Science*, 27(6):1197–1203, 1972. doi:https://doi.org/10.1016/0009-2509(72)80096-4.

This is the author's peer reviewed, accepted manuscript. However, the online version of record will be different from this version once it has been copyedited and typeset.

PLEASE CITE THIS ARTICLE AS DOI: 10.1063/1.50213744

- [20] S. Plimpton. Fast parallel algorithms for short-range molecular dynamics. *J. Comp. Phys.*, 117:1–19, 1995. doi:10.1006/jcph.1995.1039.
- [21] G. Rutkai, M. Thol, R. Span, and J. Vrabec. How well does the lennard-jones potential represent the thermodynamic properties of noble gases? *Molecular Physics*, 115(9-12):1104–1121, 2016. doi:10.1080/00268976.2016.1246760.
- [22] E.W. Lemmon, M.L. Huber, and M.O. McLinden. Reference fluid thermodynamic and transport properties-refprop. *NIST Standard Reference Database 23, Version 8.0*, National Institute of Standards and Technology, 2007.
- [23] D.O. Dunikov, S.P. Malyschenko, and V.V. Zhakhovskii. Corresponding states law and molecular dynamics simulations of the lennard-jones fluid. *J. Chemical Physics*, 115:6623, 2001. doi:https://doi.org/10.1063/1.1396674.
- [24] B. Smit. Phase diagrams of lennard-jones fluids. *The Journal of Chemical Physics*, 96(11):8639–8640, 1992. doi:10.1063/1.462271.
- [25] J. Vrabec, G. Kumar Kedia, G. Fuchs, and H. Hasse. Comprehensive study of the vapour-liquid coexistence of the truncated and shifted lennard-jones fluid including planar and spherical interface properties. *Molecular Physics*, 104(9):1509–1527, 2006. doi:10.1080/00268970600556774.
- [26] G. Nosé. A molecular dynamics method for simulations in the canonical ensemble. *Molecular Physics*, 52(2):255–268, 1984. doi:10.1080/00268978400101201.
- [27] W.G. Hoover. Canonical dynamics: Equilibrium phase-space distributions. *Physical review A*, 31(3):1695–1697, 1985. doi:10.1103/PhysRevA.31.1695.
- [28] S.W. Sides, G.S. Grest, and M. Lacasse. Capillary waves at liquid-vapor interfaces: A molecular dynamics simulation. *Physical review E*, 60(6):6708–6713, 1999. doi:10.1103/PhysRevE.60.6708.
- [29] C. Braga, E.R. Smith, A. Nold, D.N. Sibey, and S. Kalliadasis. The pressure tensor across a liquid-vapor interface. *J. Chemical Physics*, 149(044705), 2018. doi:10.1063/1.5020991.
- [30] H. Watanabe, N. Ito, and C. Hu. Phase diagram and universality of the lennard-jones gas-liquid system. *J. Chemical Physics*, 136(204102), 2012. doi:10.1063/1.4720089.
- [31] A. Trokhymchuk and J. Alejandre. Computer simulations of liquid/vapor interface in lennard-jones fluids: Some equations and answers. *J. Chemical Physics*, 111(18):8510–8523, 1999. doi:10.1063/1.480192.
- [32] H.J.C. Berendsen, J.P.M. Postma, W.F. van Gunsteren, A. DiNola, and J.R. Haak. Molecular dynamics with coupling to an external bath. *J. Chemical Physics*, 81(8):3684–3690, 1984. doi:10.1063/1.448118.
- [33] F. P. Buff, R. A. Lovett, and F. H. Stillinger. Interfacial density profile for fluids in the critical region. *Phys. Rev. Lett.*, 15:621–623, Oct 1965. doi:10.1103/PhysRevLett.15.621.
- [34] E. Chacón and P. Tarazona. Intrinsic profiles beyond the capillary wave theory: A monte carlo study. *Phys. Rev. Lett.*, 91:166103, Oct 2003. doi:10.1103/PhysRevLett.91.166103.
- [35] Pedro Tarazona, E Chacón, and Fernando Bresme. Intrinsic profiles and the structure of liquid surfaces. *Journal of physics. Condensed matter : an Institute of Physics journal*, 24:284123, 07 2012. doi:10.1088/0953-8984/24/28/284123.
- [36] P. Tarazona and E. Chacón. Monte carlo intrinsic surfaces and density profiles for liquid surfaces. *Phys. Rev. B*, 70:235407, Dec 2004. doi:10.1103/PhysRevB.70.235407.
- [37] C. W. Gardiner. *Handbook of stochastic methods for physics, chemistry and the natural sciences*, volume 13 of *Springer Series in Synergetics*. Springer-Verlag, Berlin, third edition, 2004.
- [38] G. Galliero, C. Boned, and A. Baylaucq. Molecular dynamics study of the lennard-jones fluid viscosity: application to real fluids. *Ind. Eng. Chem. Res.*, 44:6963–6972, 2005. doi:10.1021/ie050154t.
- [39] G. Burrows. Evaporation at low pressures. *Journal of Applied Chemistry*, 7(7):375–384, 1957. doi:https://doi.org/10.1002/jctb.5010070706.

This is the author's peer reviewed, accepted manuscript. However, the online version of record will be different from this version once it has been copyedited and typeset.

PLEASE CITE THIS ARTICLE AS DOI: 10.1063/5.0213744

- [40] P. Clausing. The flow of highly rarefied gases through tubes of arbitrary length. *Journal of Vacuum Science and Technology*, 8(5):636–646, 1971. doi:10.1116/1.1316379.
- [41] D. van Essen and W. Chr. Heerens. On the transmission probability for molecular gas flow through a tube. *Journal of Vacuum Science and Technology*, 13(6):1183–1187, 1976. doi:10.1116/1.569064.
- [42] Amitabh Mohan, Robert V. Tompson, and Sudarshan K. Loyalka. Efficient numerical solution of the clausung problem. *Journal of Vacuum Science & Technology A*, 25(4):758–762, 2007. doi:10.1116/1.2746875.
- [43] Donald J. Santeler. New concepts in molecular gas flow. *Journal of Vacuum Science & Technology A*, 4(3):338–343, 1986. doi:10.1116/1.573923.
- [44] A. S. Berman. Free molecule transmission probabilities. *Journal of Applied Physics*, 36(10):3356–3356, 1965. doi:10.1063/1.1702984.
- [45] Francis F. Chen. *Introduction to plasma physics and controlled fusion*, volume 1. Springer New York, NY, United States, 2010.
- [46] F. Reif. *Fundamentals of Statistical and Thermal Physics*. McGraw Hill, United States, 1965.
- [47] J. Klafter and I.M. Sokolov. *First Steps in Random Walks: From Tools to Applications*. Oxford University Press, New York, 2011.
- [48] S. Kullback and R. A. Leibler. On information and sufficiency. *The Annals of Mathematical Statistics*, 22(1):79–86, 1951.
- [49] Shen C. *Rarefied Gas Dynamics*. Springer Berlin, Heidelberg, 2005. doi:https://doi.org/10.1007/b138784.
- [50] Sergiu Busuioac, Livio Gibelli, Duncan A. Lockerby, and James E. Sprittles. Velocity distribution function of spontaneously evaporating atoms. *Phys. Rev. Fluids*, 5:103401, Oct 2020. doi:10.1103/PhysRevFluids.5.103401.
- [51] E.M. Fernández, E. Chacón, P. Tarazona, A.O. Parry, and C. Rascón. Intrinsic fluid interfaces and nonlocality. *Phys. Rev. Lett.*, 111:5, 2013. doi:10.1103/PhysRevLett.111.096104.
- [52] W. Bu, D. Kim, and D. Vaknin. Density profiles of liquid/vapor interfaces away from their critical points. *J. Phys. Chem. C*, 118(23):5, 2014. doi:10.1021/jp504374z.
- [53] J.D. Weeks. Structure and thermodynamics of the liquid–vapor interface. *Journal of Chemical Physics*, 67(7):3106, 1977. doi:https://doi.org/10.1063/1.435276.
- [54] M. Grant and R.C. Desai. Fluctuating hydrodynamics and capillary waves. *Phys. Rev. A*, 27:2577–2584, May 1983. doi:10.1103/PhysRevA.27.2577.
- [55] E.M. Blokhuis. On the spectrum of fluctuations of a liquid surface: From the molecular scale to the macroscopic scale. *The Journal of Chemical Physics*, 130(1):014706, 2009. doi:10.1063/1.3054346.
- [56] E.M. Blokhuis and D. Bedeaux. Optical properties of the fluid-fluid interface. *Physica A: Statistical Mechanics and its Applications*, 164(3):515–548, 1990. doi:https://doi.org/10.1016/0378-4371(90)90221-D.
- [57] Irina A. Graur, Elizaveta Ya. Gatapova, Moritz Wolf, and Marina A. Batueva. Non-equilibrium evaporation: 1d benchmark problem for single gas. *International Journal of Heat and Mass Transfer*, 181:121997, 2021. URL: https://www.sciencedirect.com/science/article/pii/S0017931021011030, doi:https://doi.org/10.1016/j.ijheatmasstransfer.2021.121997.
- [58] Irina A. Graur, Marina A. Batueva, Moritz Wolf, and Elizaveta Ya. Gatapova. Non-equilibrium condensation. *International Journal of Heat and Mass Transfer*, 198:123391, 2022. URL: https://www.sciencedirect.com/science/article/pii/S0017931022008602, doi:https://doi.org/10.1016/j.ijheatmasstransfer.2022.123391.